ARL-TR-9142 ● FEB 2021

# Mechanical Response and Fracture of Human Skull to Blunt Indentation Loading

by C Allan Gunnarsson, Stephen L Alexander, and Tusit Weerasooriya

## NOTICES

### Disclaimers

The research reported in this document was performed in connection with contract/instrument W911QX-16-D-0014 with the DEVCOM Army Research Laboratory.

The findings in this report are not to be construed as an official Department of the Army position unless so designated by other authorized documents. The views and conclusions contained in this document are those of SURVICE Engineering Company and the DEVCOM Army Research Laboratory

Citation of manufacturer's or trade names does not constitute an official endorsement or approval of the use thereof.

Destroy this report when it is no longer needed. Do not return it to the originator.

ARL-TR-9142 ● FEB 2021


# Mechanical Response and Fracture of Human Skull to Blunt Indentation Loading

**C Allan Gunnarsson and Tusit Weerasooriya**
*Weapons and Materials Research Directorate,*
*DEVCOM Army Research Laboratory*

**Stephen L Alexander**
*SURVICE Engineering Company*

# REPORT DOCUMENTATION PAGE

*Form Approved*
*OMB No. 0704-0188*



| 1. REPORT DATE *(DD-MM-YYYY)* | 2. REPORT TYPE | 3. DATES COVERED (From - To) |
|---|---|---|
| February 2021 | Technical Report | 1 December 2017–31 July 2019 |

**4. TITLE AND SUBTITLE**
Mechanical Response and Fracture of Human Skull to Blunt Indentation Loading

**5a. CONTRACT NUMBER**
W911QX-16-D-0014

**5b. GRANT NUMBER**

**5c. PROGRAM ELEMENT NUMBER**

**6. AUTHOR(S)**
C Allan Gunnarsson, Stephen L Alexander, and Tusit Weerasooriya

**5d. PROJECT NUMBER**

**5e. TASK NUMBER**

**5f. WORK UNIT NUMBER**

**7. PERFORMING ORGANIZATION NAME(S) AND ADDRESS(ES)**
DEVCOM Army Research Laboratory
ATTN: FCDD-RLW-PB
Aberdeen Proving Ground, MD 21005

**8. PERFORMING ORGANIZATION REPORT NUMBER**
ARL-TR-9142

**9. SPONSORING/MONITORING AGENCY NAME(S) AND ADDRESS(ES)**

**10. SPONSOR/MONITOR'S ACRONYM(S)**

**11. SPONSOR/MONITOR'S REPORT NUMBER(S)**

**12. DISTRIBUTION/AVAILABILITY STATEMENT**
Approved for public release: distribution unlimited.

**13. SUPPLEMENTARY NOTES**
ORCID ID(s): Tusit Weerasooriya, 0000-0003-3299-2166; C Allan Gunnarsson, 0000-0002-8472-5193

**14. ABSTRACT**
Behind-helmet blunt trauma (BHBT) events transfer energy to the skull and brain, leading to injuries such as skull fracture and traumatic brain injury. The presence of a cranial fracture has been shown to be associated with a higher incidence of intracranial lesions, neurological deficit, and poorer medical outcomes. Therefore, it is important to understand the effect of blunt indentation loading on skull deformation and fracture. Human skullcap specimens were fabricated from postmortem human subjects. They were loaded to replicate blunt impact at both low and high loading rate to quantify the skull mechanical deformation response, as well as associated damage and fracture initiation mechanisms. The specimens were characterized using high-resolution microcomputed tomography (25-µm voxel resolution) to understand structural deformation, damage, and fracture that occurred in the skullcap specimen during loading. These experimental measurements are used to understand the mechanical response and include subsequent fracture initiation of the complex 3-D human skull structures. The data and insight gained from this study have been used to develop deformation and failure criteria for use in computational models, in addition to validation of material model and computational methods.

**15. SUBJECT TERMS**
high-rate loading and digital image correlation, indentation and impact loading of human skull, human skull mechanical behavior, human skull fracture, backface deformation, split Hopkinson pressure bar (SHPB), Kolsky bar, computed tomography

| 16. SECURITY CLASSIFICATION OF: | | | 17. LIMITATION OF ABSTRACT | 18. NUMBER OF PAGES | 19a. NAME OF RESPONSIBLE PERSON |
|---|---|---|---|---|---|
| a. REPORT | b. ABSTRACT | c. THIS PAGE | | | C Allan Gunnarsson |
| Unclassified | Unclassified | Unclassified | UU | 58 | 19b. TELEPHONE NUMBER (Include area code) (410) 306-1964 |

## Contents

## List of Figures

## List of Tables

## Acknowledgments

The authors would like to acknowledge the contributions of the following US Army Combat Capabilities Development Command Army Research Laboratory researchers to this study: Jessica Sun and Timothy Walter for conducting microcomputed tomography (micro-CT) scans of the post- and pretested skullcap specimens; Karin Rafaels for procuring postmortem human skulls and fabrication of experimental specimens; and Erika Matheis for fabrication of the experimental specimens. The authors also acknowledge the contributions of Panagiotis (Pete) Saliaris, who helped identify the fracture patterns in the pre- and post-loaded skullcap micro-CT images during his time in the laboratory as a summer intern.

# 1. Introduction

Understanding and mitigating head injuries are important goals among the defense research community. Over 235,000 service members were diagnosed with traumatic brain injury (TBI) from 2000 to 2011, and it is estimated that 1.7 million civilians sustain a TBI each year (Multi-agency Leadership Panel 2013). TBI can occur when external mechanical forces act on the head. These applied forces affect pressure and strain in the hard and soft tissues of the skull and brain. These mechanical forces may be present during behind-helmet blunt trauma (BHBT) events, which occur when a projectile strikes the head protection device, such as a helmet, causing the device to deform and contact the head. Understanding the underlying mechanisms of head injury by these mechanical forces enables the design of better head protection concepts and devices. Therefore, it is necessary to understand how blunt indentation loading affects the skull.

Determination of mechanical thresholds (pressure, strain, etc.) in brain cells and tissues that lead to TBI of varying intensity is being studied with some success (Meaney et al. 2014). The presence of skull fracture has been established as an indicator of reduced medical outcomes and increased likelihood of TBI (Bullock et al. 2006; Tseng et al. 2011). Therefore, understanding the deformation and fracture behavior of the skull will enable researchers to incorporate mechanical threshold–based injury models into computational concepts in order to predict skull fracture and the increased likelihood of brain injury during computer simulation of BHBT events.

There are no known experimental studies focused on how the skull deforms and fractures during blunt loading, which would allow incorporation of fracture mechanism–based injury threshold models into computational methods to accurately predict skull behavior during blunt indentation loading. Ritchie et al. (2005) discussed the fracture behavior of bone and put forth several toughening mechanisms that occur in cortical bone, including osteon deflection, microcracking, uncracked ligament bridging, and collagen fiber crack bridging. However, many of these apply to the highly oriented cortical bone present in load-bearing bones.

The mechanical response of the adult human skull during bending has been investigated using thin skull beam specimens loaded in three-point bending (Hubbard 1971; Verschueren et al. 2006; Delille et al. 2007; Motherway et al. 2009; Rahmoun et al. 2014; Gunnarsson et al. 2021). They found that fracture initiation occurred in tension on the inner surface of the specimens, with elastic moduli ranging from 2.3 ± 1.2 GPa (Verschueren et al. 2006) to 9.69 ± 2.32 GPa (Hubbard 1971). During BHBT events, however, the skull directly under the loading point

has full 3-D shape and structure, which differs from the thin beam geometry in these bend studies; thus, the deformation and fracture response of thin skull beams are likely different from that of the full 3-D skull.

Other studies have characterized the mechanical response of the skull in different loading configurations for human (McElhaney et al. 1970; Wood 1971; Peterson and Dechow 2003; Boruah et al. 2013; Boruah et al. 2017; Brown et al. 2021; Alexander et al. 2020a), large-breed porcine (Margulies and Thibault 2000; Baumer et al. 2009), miniature Gottingen porcine (Alexander et al. 2019a), and miniature Yucatan porcine (Gunnarsson et al. 2018) species. The authors are not aware of any existing skullcap indentation loading experimental studies, which represent more realistic BHBT loading of the 3-D skull.

The macroscopic structure of the human skull has been reported (Gibson and Ashby 1997) and microstructurally quantified in great detail (Alexander et al. 2019b). Based on extensive measurements of porosity distributions, Alexander et al. divided the skull bone structure into a three-layer system with outer table (OT), mid-diploe (MD), and inner table (IT) based on a 30% porosity threshold. Their method considered denser cortical (compact) bone in the OT and IT to have porosity below 30%, and the more porous trabecular (spongy) bone in the MD to have porosity greater than 30%. The degree of structural anisotropy in mature cranial human bone has also been characterized (Dempster 1967; McElhaney et al. 1970). Some studies have classified cranial human bone as structurally isotropic, indicating that there is no prevailing directional bias in the arrangement of the bone. Dempster punctured decalcified human skull away from the orbital cavities and facial structures to visualize the dominant direction of collagenous fibers in the outer table. He concluded that the fibers had a random orientation in the skull. Similarly, McElhaney et al. (1970) could not discern dominant directions in the histology of each of the three cranial layers. These findings are supported by recent observations (Alexander et al. 2019b) that used high-resolution microcomputed tomography (micro-CT) visualization of the canal structure within the tables of the human skull. This lack of a dominant structural direction in cranial bone is in sharp contrast to load-bearing bones, such as the femur, which possess a highly anisotropic substructure and have shown mechanical response and fracture behavior to be highly dependent on loading orientation (Sanborn et al. 2016; Weerasooriya et al. 2016).

The development of head protection devices includes evaluating the impact response on postmortem human subjects (PMHS) to understand the protection level provided. During posttest evaluation, the PMHS heads are autopsied; one metric used to evaluate the performance of the device is the presence and intensity of macroscale skull fracture. However, during these full head BHBT experiments, it

is impossible to quantify the exact load applied to the skull and how much it deforms. The purpose of this study is to reduce the experimental length scale down to the skullcap size, allowing for quantification of specimen load history, deformation history, and fracture, while maintaining the full 3-D structure of the skull and loading conditions that approximate the geometry of BHBT events.

It is known that the geometry of helmet deformation during ballistic impact is quite blunt relative to the geometry of the projectile (Hisley et al. 2011), where the deformed helmet radius of curvature is much greater than that of the projectile. Others have conducted full head protection evaluation experiments with the goal of determining head injury to BHBT events using PMHS (Matheis et al. 2019) and live animal surrogates (Ivancik et al. 2018), with flash X-ray imaging of the head and head protection (helmet) during impact. Figure 1 presents an unpublished sample X-ray image from one BHBT experiment (Matheis et al. 2019), showing the head, deformed head protection (helmet), and projectile at some time after impact. After impact, the helmet deforms and may contact the head. The geometry of the helmet back-surface when it contacts the head has a large curvature and is much blunter relative to the original projectile geometry.

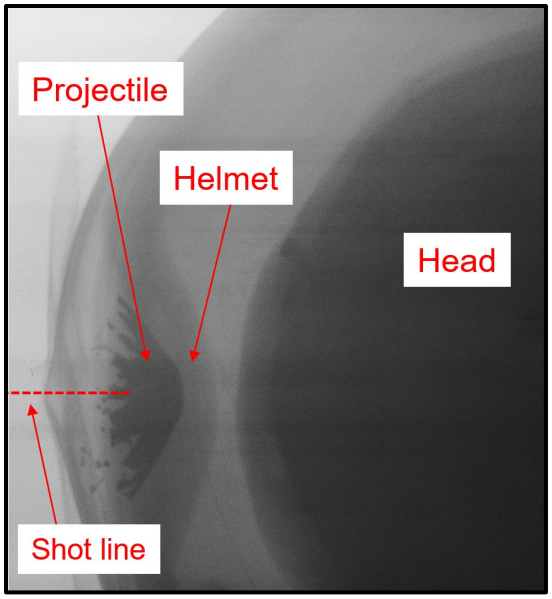


**Fig. 1 BHBT experimental X-ray image during impact, indicating large curvature for helmet back-surface as it impacts the head (Matheis et al. 2019)**

In this study, the deformation and fracture of the human skull by blunt indentation loading was investigated. Skullcap specimens were fabricated from adult PMHS skulls. The structure of the specimens was scanned using high spatial resolution (~25-μm voxel size) micro-CT prior to loading. The skullcap specimens were loaded to represent BHBT events. During loading, the skull specimen inner surface

was speckled and the motion was recorded, allowing for the use of digital image correlation (DIC) to quantify the full-field deformation of the inner surface during loading. Prior to or just after failure, loading was removed, and the skull structure was again scanned with the micro-CT. This posttest micro-CT scan allowed for a direct comparison with the pretest micro-CT scan, identifying the effect of loading on the skull structure and allowing for observation of fracture at the microstructure scale. The results of this study are used to understand human skull deformation and fracture mechanisms in response to blunt indentation loading so that they may be incorporated into computational modeling of head impact events (Alexander et al. 2020b; Weerasooriya and Alexander 2020).

## 2. Methods

Adult human porous skull bone can be represented as a three-layer sandwich structure with inner and outer tables composed of dense (low porosity) cortical bone sandwiched around a middle layer, the diploe, which is a highly porous trabecular bone. One method for classifying skull bone as either cortical or trabecular is based on the porosity of the tissue (Alexander et al. 2019b). As discussed before, Alexander et al. defined cortical (compact) bone to be denser, with porosity below 30%, and trabecular (spongy) bone to be less dense, with porosity greater than 30%.

### 2.1 Human Skullcap Specimens

The experiments reported here were conducted in compliance with the US Army Combat Capabilities Development Command Army Research Laboratory Policy for Use of Human Cadavers for Research, Development, Test, and Evaluation under the guidance and oversight of the DEVCOM ARL Human Cadaver Review Board and the ARL Safety Office. The skullcap specimens were extracted and fabricated from the skulls of adult PMHS. A handheld bone saw was used to cut the skull approximately at the ear line; a bone pathology saw (Exact 312, Exact Technologies, Inc.) was then used to cut this upper skull (Fig. 2a, right) to fabricate the skullcap specimen (Fig. 2a, left).

The skullcap specimen was dome-shaped (Fig. 2). The specimen outer surface is the outer bound of the OT region and was nearest to the scalp (Fig. 2a left); this is also referred to as the top of the skullcap specimen. The bottom surface of the skullcap specimen (Fig. 2b) consisted of both the inner surface (nearest to the brain) and the cut surface. The inner surface is bounded by the light pencil-marked contour in Fig. 2b. The approximate center of the inner surface is identified in Fig. 2b. The loading point is the location that the indenter tip contacts the skullcap on the outer

surface and was chosen so the loading axis passes through the center of the inner surface.

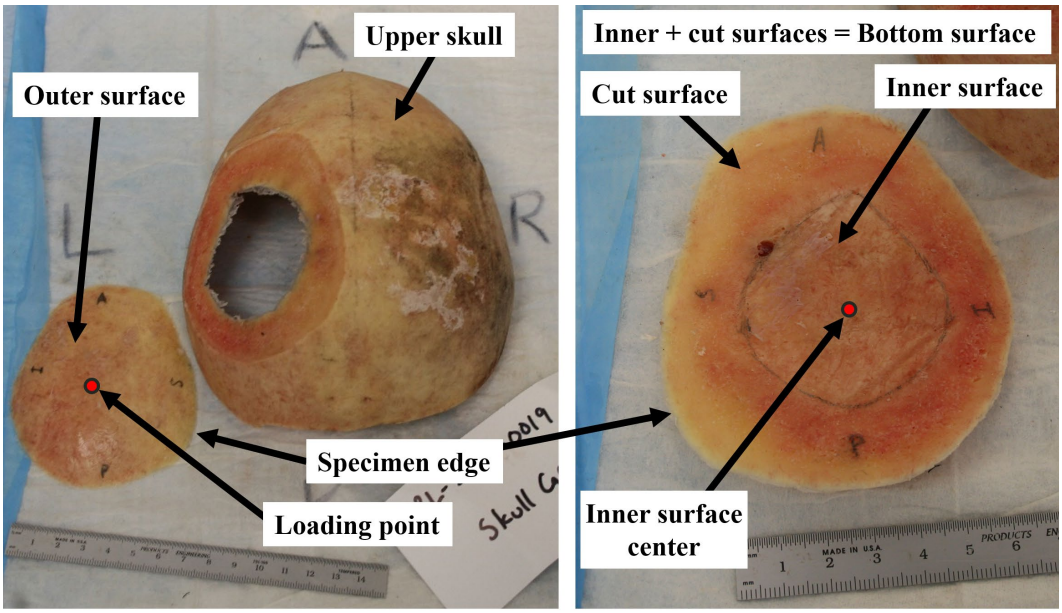


**Fig. 2 (a) Top view of human skullcap specimen ARL-2017-0019-LPAR (left) cut from PMHS upper skull (right) and (b) bottom view of skullcap specimen ARL-2017-0019-LPAR showing the inner surface and the cut surface. Numbered divisions on both scales are in centimeters.**

The bottom surface between the pencil mark and the specimen edge is referred to as the cut surface; this surface contains the skull through-thickness. That is, the cut surface consists of IT, diploe, and OT as it proceeds from the inner surface–cut surface boundary (pencil mark) to the specimen edge. Specimen edge refers to the location where the outer surface and cut surface meet. Labels were used to identify the orientation of the skullcap specimen relative to the donor skull/head. These include A, P, S, I, L, and R, corresponding to the anterior, posterior, superior, inferior, left, and right directions, respectively.

The skullcap specimens were cut from the upper skull so that the coronal and sagittal sutures (which separate the frontal and parietal bones, and the two parietal bones, respectively) were not present in the skullcap specimens. After cutting, the skullcap specimens were hand wet-sanded until the cut surface was flat to ensure uniform contact between the specimen cut surface and the backing plate (also referred to as mounting plate) everywhere along the cut surface. The specimens were approximately 75–150 mm across after fabrication. Their shape varied; some were almost round while others were irregularly shaped.

The distance between the inner and outer surfaces along the *y*-axis at the loading point is considered the specimen thickness (Fig. 3a). This distance was not constant over the entire specimen. The specimen height is the distance between the loading point and the cut surface along the *y*-axis (Fig. 3a). The specimens were stored frozen after fabrication. Prior to micro-CT scanning or testing, the specimens were thawed to room temperature and hydrated in Hank's Balanced Salt Solution (HBSS). For mechanical loading, the specimens were removed from HBSS and blotted dry on the inner surface to eliminate any fluid. After testing, the specimens were immediately returned to frozen storage.

The individual specimens were identified with the format ARL-YEAR-XXXX-BONE. YEAR identified the year the PMHS donor arrived at ARL, XXXX indicated the donor number, and BONE indicated the skull bone that the skullcap specimen was cut from. The left and right parietal bones were represented by LPAR and RPAR, respectively, and FRONTAL was used for the frontal bone. In addition, a shorthand notation, referred to as the specimen code, with the format XR-## was used throughout for brevity. In the specimen code, X represents the loading rate, with L used for quasi-static (low) rate, and H used for high rate; ## represents the skullcap specimen number, here spanning 01 to 10.

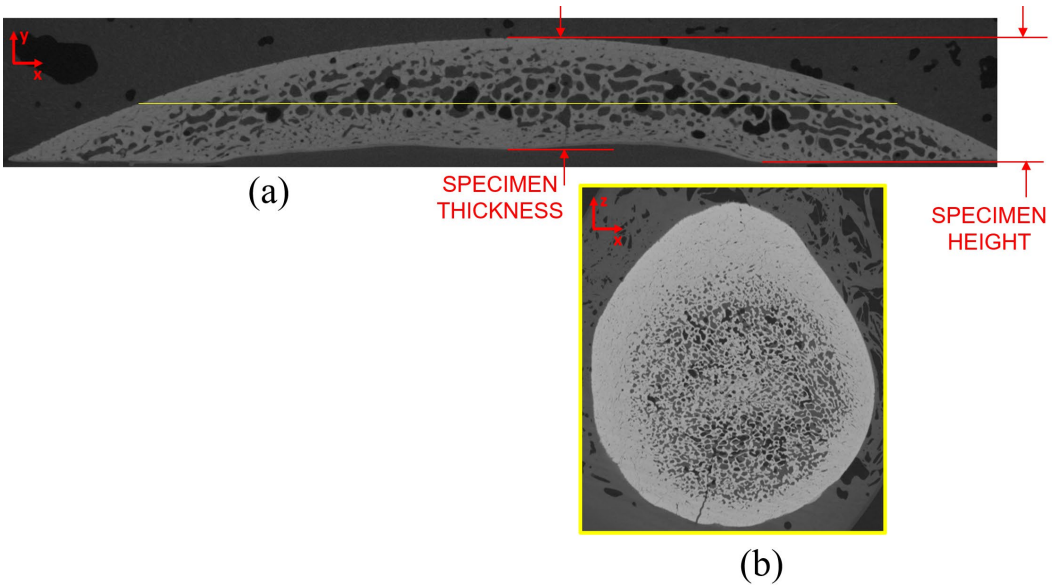


**Fig. 3 Example of micro-CT data from LR03 (posttest), with (a) cross-section image (*x*-*y* plane) and (b) stack image (*x*-*z* plane) with yellow line. The yellow line in (a) indicates the *y* location of (b). Note the presence of edge macro-fracture in (b).**

## 2.2 Microcomputed Tomography

The skullcap specimen geometry and microstructure were quantified using a micro-CT scanner (Northstar XRD 1620) with an isotropic voxel size of 24–26 µm;

X-ray source settings of 160 kV and 260 µA (41.6 W) with no filter were used for all specimens. The specimens were placed inside a plastic container and wrapped in HBSS-saturated gauze to maintain hydration during micro-CT scanning. Each specimen was micro-CT scanned pre- and posttest to allow for the effect of loading on structure to be quantified. The pre- and posttest scan datasets were registered using a difference minimization algorithm, to rotate and align the two datasets so that differences in scan orientation are minimized.

The micro-CT scan images were reconstructed into an image stack along the thickness dimension (*y*-axis) at the loading point. Figure 3b shows an example of a stack image (*x*-*z* plane), along with a representative cross-sectional view (*x*-*y* plane) in Fig. 3a. In the cross-sectional view (Fig. 3a), the yellow line represents the approximate *y*-axis location of the stack image (Fig. 3b). Here, black represents air/pore and gray represents bone.

## 2.3 Blunt Indentation Loading Experiments

For the blunt indentation loading experiments documented here, the skullcap specimens were loaded using a hemispherical-shaped indenter tip with tip diameter of 31.75 mm (1.25 inches). This indenter geometry was chosen to approximate the blunt impact geometry observed in BHBT experiments, as discussed previously. A backing plate was used to support the cut surface of the specimen during loading. A cutout in the backing plate, with identical shape to the specimen inner surface, allowed for direct observation of the specimen inner surface backface deformation (BFD) along the loading axis during loading by the digital cameras; this required machining a different backing plate for each specimen to match the outline of the inner surface shape of each specimen. A schematic of the loading configuration is shown in Fig. 4.

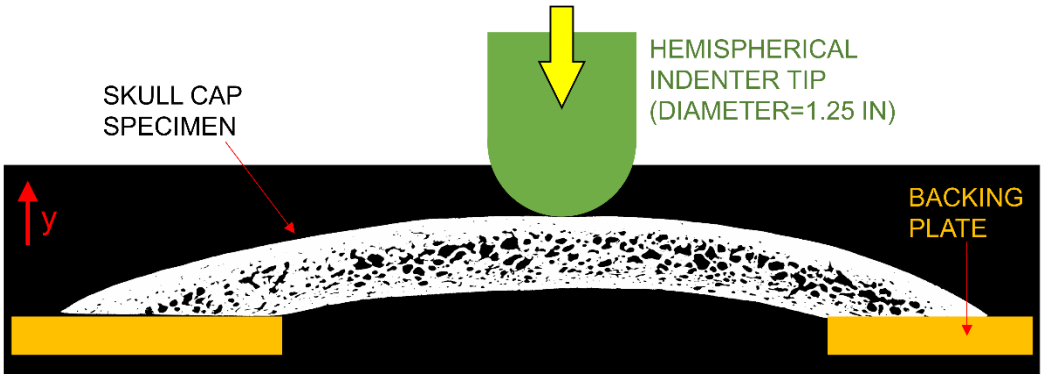


**Fig. 4 Loading schematic for blunt indentation loading (specimen LR03 shown)**

Blunt indentation loading experiments were performed at two different loading rates, high rate and quasi-static rate, using similar indenter tips (identical geometry made of different materials as detailed below). The high-rate loading experiments were performed using a modified split Hopkinson pressure bar (SHPB) setup. The quasi-static rate loading experiments were performed using a standard hydraulic test machine (Instron 8871). For both loading rates, 3-D DIC was performed on the speckled specimen inner surface, through the backing plate cutout to quantify full-field inner surface BFD. For all experiments, the DIC displacement data was coordinate transformed to ensure that the specimen inner surface BFD measurement axis was parallel to the loading axis ($y$-axis in Fig. 4). Using 2-D DIC, a third camera captured indenter tip displacement during loading to correct for any machine compliance.

For these experiments, the objective was to observe the location of micro-fracture initiation or damage prior to macro or catastrophic fracture; here defined as a visible fracture present through the specimen thickness with significant length. For several of these experiments, the load was removed prior to macro-fracture once softening was observed in real time in an attempt to observe micro-fracture initiation at or near the loading point through posttest micro-CT imaging.

### 2.3.1 High Loading Rate Experiments

High-rate indentation loading experiments were performed using a modified SHPB setup, consisting of a traditional incident bar with a hemispherical indenter tip. The incident bar and indenter tip were made of Al-7075, with a diameter of 31.75 mm (1.25 inches). The indenter tip was attached to the incident bar using a plastic sleeve and had a tip diameter of 31.75 mm (1.25 inches). The plastic sleeve connected the indenter tip and incident bar with a tight sliding fit; both were free to slide through the sleeve. Instead of a traditional transmission bar, the specimens were supported by a backing plate normal to the incident bar axis; this configuration allowed the specimens to expand radially. The backing plate was made of polycarbonate and mounted to a rigid aluminum frame. High-speed cameras (Photron SA5, 50,000 fps) recorded the speckled skull specimen inner surface during loading. This allowed for measurement of the full-field BFD profile of the skull inner surface during load using DIC. A side view high-speed camera captured the bar end and indenter tip motion (Photron APX-RS, 50,000 fps), as the indenter tip was not rigidly mounted to the bar end. A schematic of the high-rate loading experimental setup is shown in Fig. 5a, while the actual experimental setup is shown in Fig. 5b.

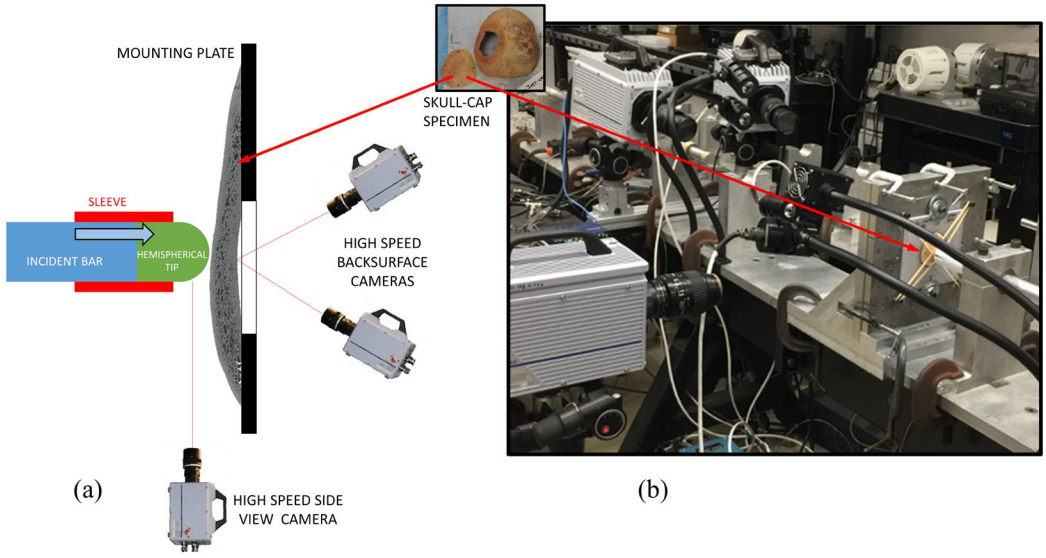


**Fig. 5 High-rate loading (a) schematic and (b) setup. The incident bar and indenter tip were Al-7075, 1.25-inch diameter; the indenter tip was hemispherical, also with 1.25-inch diameter. The backing (mounting) plate was made of polycarbonate.**

During traditional SHPB experiments, the stress waves are reflected along the bars many times, which can cause multiple loadings of the specimen. This is generally not a concern for traditional material characterization, as only the first set of pulses are used in analysis to determine the material deformation response. However, here the loading history is being related to the specimen damage observed in posttest micro-CT imaging. Therefore, a single loading momentum trap setup, similar to one proposed by Nemat-Nasser et al. (1991), was used to prevent multiple loadings of the skullcap specimen. This setup consisted of a flange threaded onto the incident bar at the striker end and a large sliding reaction mass. A preset gap, created using a micrometer drive, between the incident bar flange and reaction mass controlled the amount of incident bar motion toward the specimen.

### 2.3.2 Quasi-static Loading Rate Experiments

In addition to high loading rate experiments, quasi-static, or low, loading rate indentation experiments were also conducted. The purpose for reducing the loading rate to quasi-static was to allow for greater control and the ability to unload the specimen just as fracture initiated. Conducting indentation experiments at a quasi-static loading rate provided an opportunity for the specimens to be immediately unloaded after any indication of fracture initiation occurred in real time. This indication could happen in several ways, such as visually, if crack growth was stable and slow, popping sound or other audible cues, or by real-time observation of softening in the mechanical response.

Quasi-static loading rate experiments were performed using a hydraulic test machine (Instron 8871), with the indenter tip connected directly to the machine actuator. For quasi-static experiments, the indenter tip was a 1.25-inch-diameter hemisphere made from high-hardness tool steel. The specimen backing plate was made out of aluminum and was suspended above a mirror enabling a pair of high-resolution framing cameras (FLIR, 12.3 MP) to record images of the specimen inner surface and backing plate during loading. An additional camera was also used to record images of the indenter motion to correct for any compliance present in the loading train. Subsequent quasi-static experiments also used a single high-speed camera (Photron SA-5, 100,000 fps) positioned between the two framing cameras. This high-speed camera also recorded the specimen inner surface during loading and was used to determine the fracture initiation location. All quasi-static rate experiments were conducted at a constant displacement rate of 0.005 mm/s (0.012 inches/min). A schematic of the quasi-static rate loading experimental setup is shown in Fig. 6, along with the actual experimental setup. Two types of experiments were performed at a quasi-static loading rate: single loading and multiple loading. The multiple loading experiments used repeated load–unload–scan cycles in an attempt to capture micro-fracture initiation.

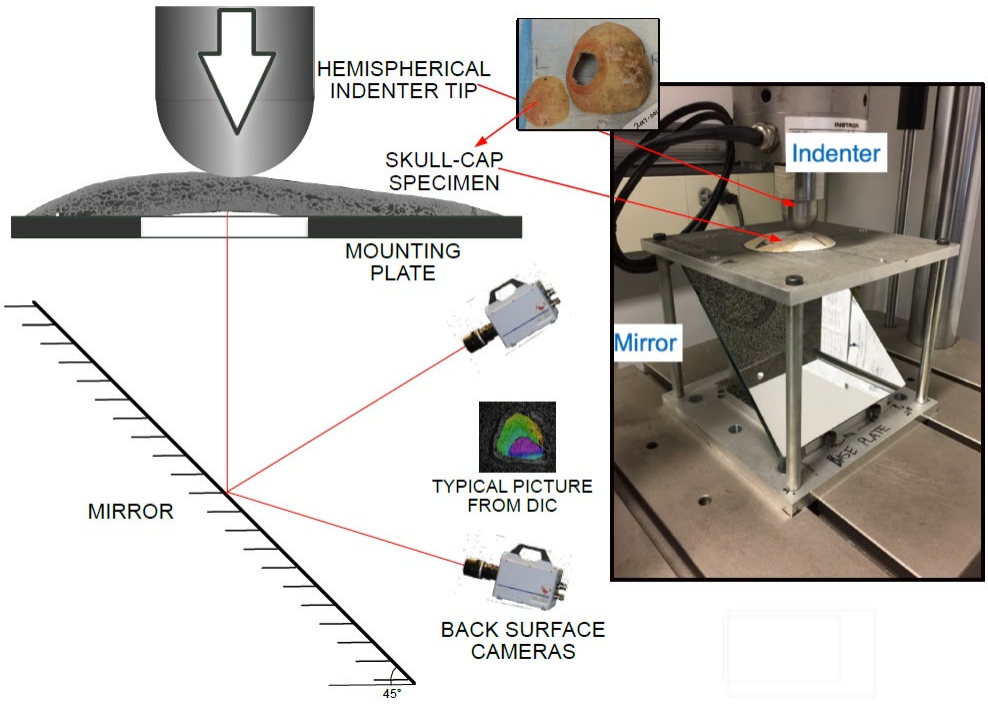


**Fig. 6 Quasi-static rate loading schematic and experimental setup. The indenter tip was a 1.25-inch-diameter hemisphere made of high-hardness tool steel, and the backing (mounting) plate was made of Al-7075.**

#### 2.3.2.1 Single Loading Experiments

For single loading experiments, the specimen was loaded one time until visual fracture or damage of some type occurred, or was indicated by softening, where the load stopped increasing and reached a plateau. There were five single loading specimens: LR03, LR05, LR06, LR07, and LR10.

#### 2.3.2.2 Multiple Loading Experiments

The multiple loading experiments consisted of several load–unload–scan cycles performed on the skullcap; the target load was incrementally increased for each cycle. First, prior to loading, the specimen was micro-CT scanned to obtain a pretest micro-CT scan dataset. Next, it was loaded to the initial target load and then immediately unloaded. The specimen was then micro-CT scanned to determine occurrence of any fracture initiation. If there was no evidence found of fracture or damage, the process was repeated, incrementally increasing the target load until fracture occurred. There were two multiple loading specimens: LR04, which was loaded for nine cycles, and LR08, which was loaded for two cycles.

### 2.3.3 Backing Plate Deformation and Apparent Stiffness

During loading, the specimen backing plate was not perfectly rigid and experienced elastic deformation. Therefore, not all of the indenter displacement was translated into specimen deformation. To obtain the actual deformation of the specimen, the raw indenter displacement was corrected by removing the elastic deformation of the bottom surface of the plate. The plate deformation was obtained from an average of points extracted around the cutout edge, as the cutout of the plate was of irregular shape. This average plate deformation was then subtracted from the raw indenter displacement to obtain the corrected indenter displacement. Figure 7 illustrates the effect of the plate deformation using the experimental data from LR08 loading cycle 02. Figure 7a shows a representative DIC contour of the out-of-plane deformation of the plate, including the 10 data extraction points (white dots) located around the plate cutout edge used to create the plate deformation measurement. Figure 7b shows the out-of-plane deformation for the 10 data points used around the plate cutout edge, as well as the load history, which illustrates minimal variability of plate deformation based on location around the plate cutout edge. Figure 7c shows the raw indenter displacement obtained from the test machine, the average plate deformation (obtained by averaging the 10 cutout edge points shown in Fig. 7b), and the corrected indenter displacement, which is obtained by subtracting the average plate deformation from the raw indenter displacement. The average plate deformation is approximately 20%–30% of the raw indenter displacement.

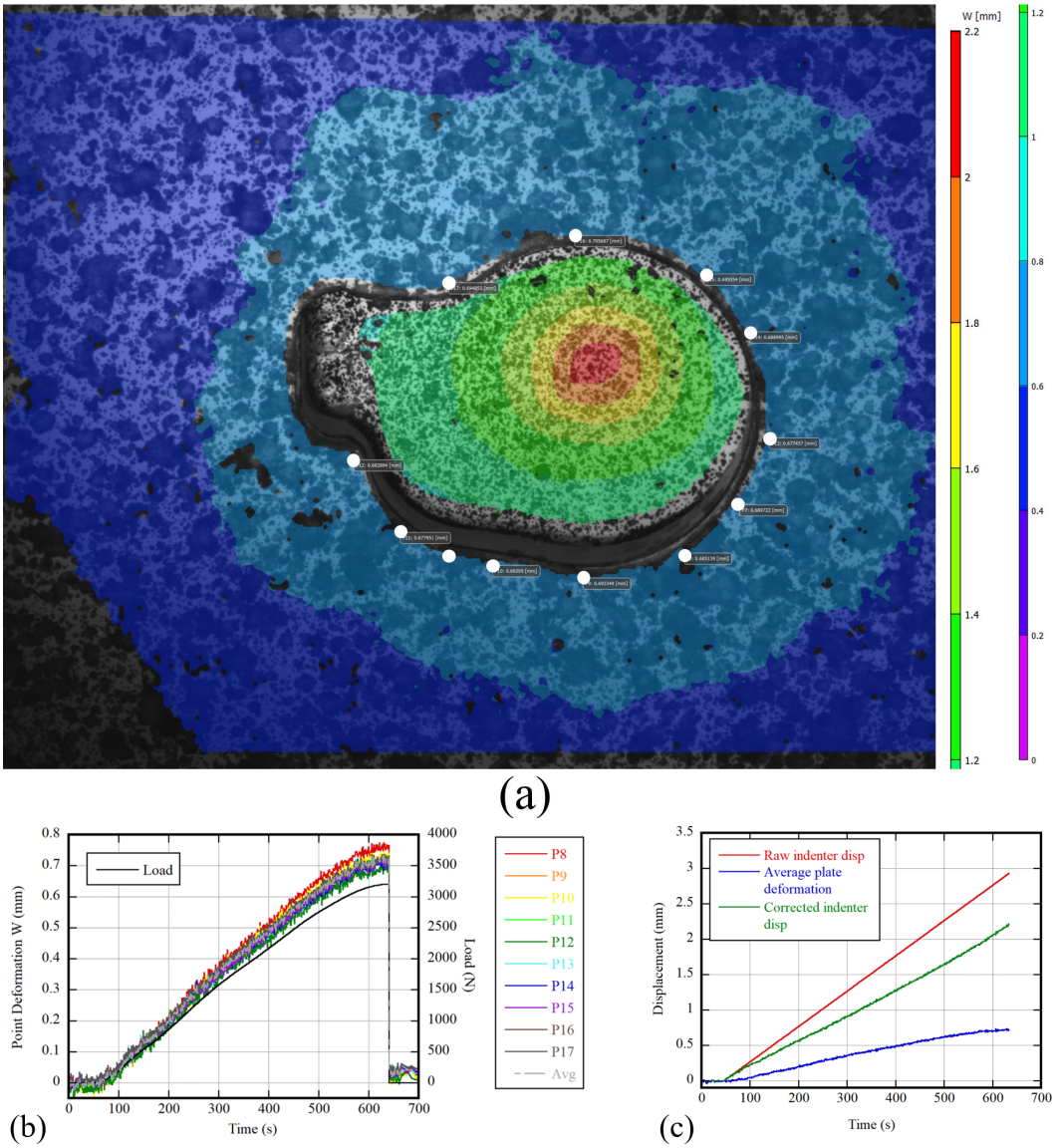


**Fig. 7 For LR08 loading cycle 02: (a) backing plate out-of-plane deformation DIC contour with data points used for average plate deformation at time just prior to fracture, (b) variability of backing plate data points based on position around cutout edge, (c) raw and corrected indenter displacement, average plate deformation**

The apparent stiffness of each skullcap was calculated by applying a linear fit to the initial portion of the specimen load–corrected indenter displacement data. This apparent stiffness represents an approximation of the structural stiffness of the skull; that is, how much load is required to deform the outer surface a certain displacement. For the quasi-static rate experiments, only the initial linear loading history was used to determine the apparent stiffness, between approximately 0.5 and 1.0 kN. For the high-rate experiments, the entire loading history up to fracture (max) load was used.

## 3. Results

The following sections detail the mechanical response and fracture behavior of the skullcap specimen experiments. Table 1 provides a summary of these results, including specimen apparent stiffness calculated using the corrected indenter displacement.

**Table 1 Experimental result summary**

| Specimen code | Specimen ID | Loading rate | No. of loading cycles | Apparent stiffness (kN/mm) | Fracture load (kN) | Loading rate (kN/s) |
|---|---|---|---|---|---|---|
| HR01 | ARL-2016-0011-FRONTAL | High | 1 | 4.453 | 3.939 | 16923 |
| HR02 | ARL-2016-0011-LPAR | High | 1 | 4.066 | 1.9645 | 7578.1 |
| LR03 | ARL-2017-0019-LPAR | Quasi-static | 1 | 1.993 | 2.412 | 0.00756 |
| LR04 | ARL-2013-0007-LPAR | Quasi-static | 9 | 2.258 | N/A | 0.0084 |
| LR05 | ARL-2017-0015-LPAR | Quasi-static | 1 | 2.159 | 3.389 | 0.00695 |
| LR06 | ARL-2017-0020-RPAR | Quasi-static | 1 | 2.05 | 2.063 | 0.007063 |
| LR07 | ARL-2017-0014-FRONTAL | Quasi-static | 1 | 2.671 | 3.758 | 0.00887 |
| LR08 | ARL-2017-0016-RPAR | Quasi-static | 2 | 2.162 | 3.205 | 0.00726 |
| LR10 | ARL-2017-0020-FRONTAL | Quasi-static | 1 | 2.299 | 1.617 | 0.00729 |

### 3.1 High-Rate Experiments

Two skullcap specimens were loaded at high rate using the modified SHPB setup. Both specimens exhibited brittle mechanical response with loading followed by fracture initiation. There was little to no permanent deformation around the loading point, such as denting or cupping, and the specimen height was approximately unchanged.

HR01 (ARL-2016-0011-FRONTAL) was loaded at 4.1 m/s for 0.80 mm, with a corresponding loading rate of 16.9 MN/s, maximum load of 3.94 kN, and apparent stiffness of 4.453 kN/mm. This specimen broke into two separate pieces, shown in Fig. 11a.

For HR02 (ARL-2016-0011-LPAR), the bar end velocity and total displacement were reduced with the goal of preventing macro-fracture while still creating fracture initiation. The velocity and displacement used for HR02 was 3.8 m/s and 0.45 mm, corresponding to a loading rate of 7.58 MN/s, a maximum load of 1.96 kN, and an apparent stiffness of 4.066 kN/mm. This specimen experienced micro-fracture initiation but did not experience macro-fracture.

### 3.1.1 Mechanical Response

The loading histories for both high-rate specimens are shown in Fig. 8. The load signals were small for this large-diameter bar with traditional strain gages. The use of higher-sensitivity semiconductor strain gages or embedded dynamic load cells would increase the signal-to-noise ratio of the load data.

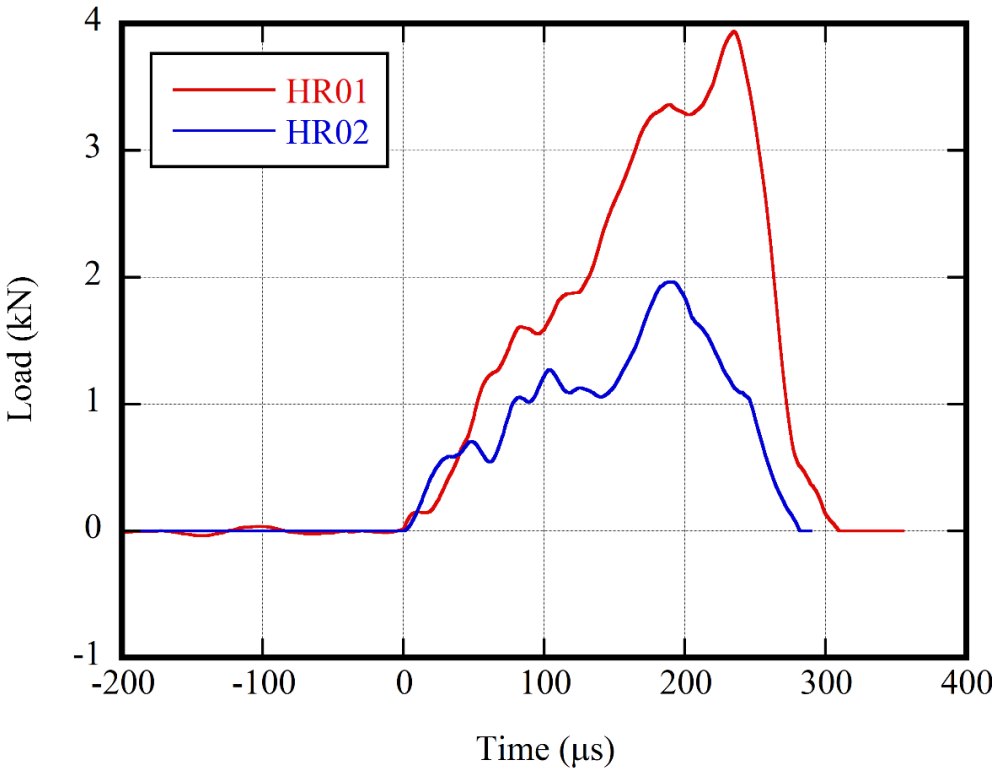


**Fig. 8 Loading history of high-rate experiments**

For the high-rate experiments, the raw indenter displacement was measured in two ways: using DIC of the speckled indenter tip and bar end motion, and using traditional SHPB analysis of the bar strain gage data. The two indenter displacement measures are virtually identical, as shown in Figs. 9a and 10a. The indenter tip displacement is higher than the bar end displacement at the end of both high-rate experiments; this is due to the indenter tip not being rigidly affixed to the bar end, which allows the indenter to continue to move toward the specimen.

The loading history for HR01 is shown, along with the corrected indenter displacement, corrected bar end displacement, and the specimen inner surface BFD at the loading point in Fig. 9a. The load-corrected indenter displacement data, used to measure apparent stiffness, is shown in Fig. 9b. The BFD at the loading point is approximately equal to the corrected indenter tip displacement, indicating that the inner and outer surface experienced the same deformation and there was no compression between the two surfaces.

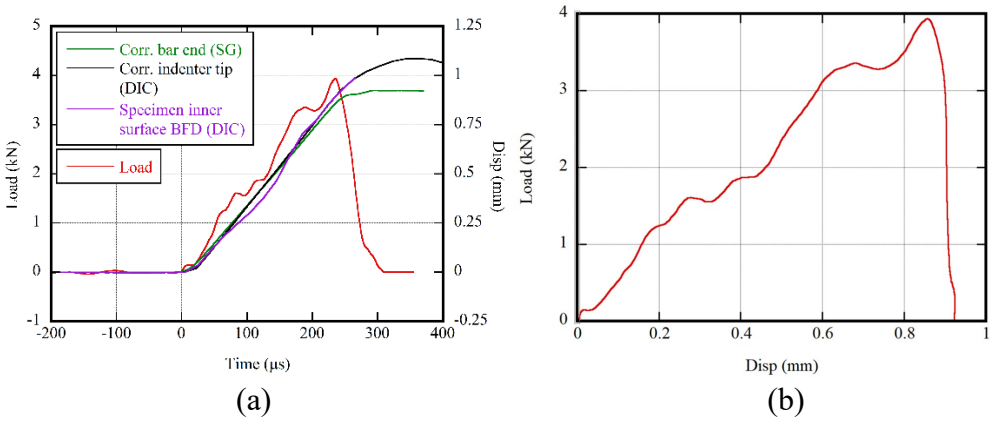


**Fig. 9 (a) Experimental data time histories for load, corrected bar end and corrected indenter tip displacements, and specimen inner surface BFD and (b) load-corrected indenter displacement history for HR01**

The loading history for HR02 is shown, along with the corrected indenter displacement, corrected bar end displacement, and the specimen BFD at the loading point in Fig. 10a. The load-corrected indenter displacement data, used for measurement of apparent stiffness, is shown in Fig. 10b. The specimen BFD at the loading point is approximately equal to the corrected indenter tip displacement, indicating that the inner and outer surface experienced the same deformation and there was no compression between the two surfaces.

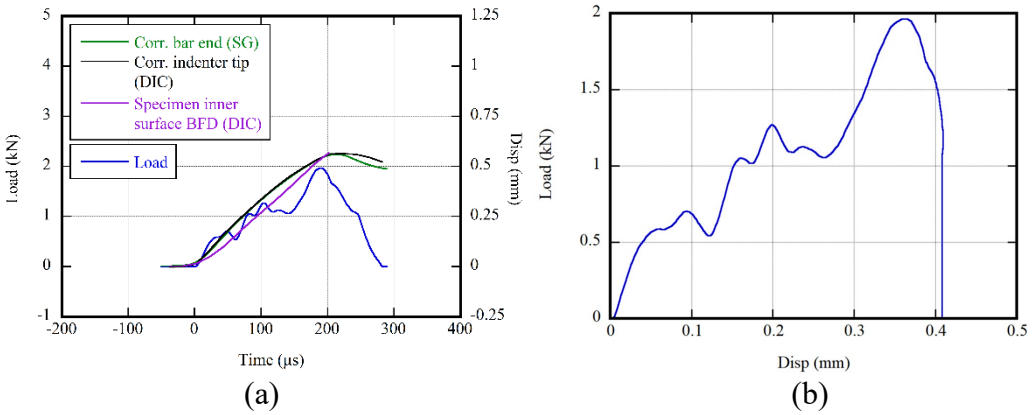


**Fig. 10 (a) Experimental data time histories for load, corrected bar end and corrected indenter tip displacements, and specimen inner surface BFD and (b) load-displacement using the indenter corrected displacement history for HR02**

### 3.1.2 Fracture Response

The two high-rate experiments experienced different levels of fracture. HR01 experienced macro-fracture and separated into two pieces. The high-speed imaging showed that fracture initiated at the specimen I-R edge, propagated through the loading point and then to the I-L edge. In addition, a secondary crack was observed, traveling from the loading point and running approximately halfway toward the S edge, indicated by the red arrow in Fig. 11a. It could not be determined when the secondary crack initiated; however, the posttest scan visualization confirmed that the crack was arrested and did not propagate to the specimen edge.

The second specimen, HR02, did not have visible macro-fracture. The posttest micro-CT scan (Fig. 11b) showed two nonvisible edge micro-fractures, with the length approximately one-third of the distance between the edge and loading point.

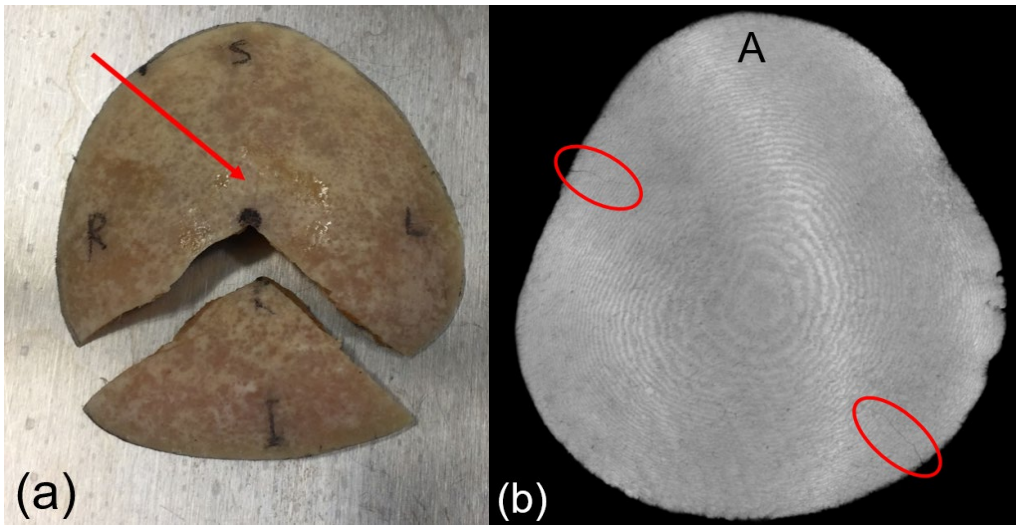


**Fig. 11 Post-experiment images of (a) HR01 (visual) and (b) HR02 (micro-CT)**

There was also micro-fracture observed directly under the loading point for HR02. In Fig. 12, showing the posttest micro-CT scan of HR02, fracture is indicated in the yellow highlighted areas. A comparison of the pre- and posttest micro-CT scans is shown in Fig. 13, which shows the same through-thickness slice for both the pre- and posttest scans shown in Fig 12. The fracture is clearly visible in the posttest image but absent from the pretest image. It was difficult to distinguish the micro-fracture from the natural structure of the skull, and it would have been impossible without having both pre- and posttest micro-CT scans available for direct comparison. Circular markers have been added to highlight common features in both scans. Having several common features demonstrates that the micro-CT slices from both datasets are approximately located at the same thickness location and are planar.

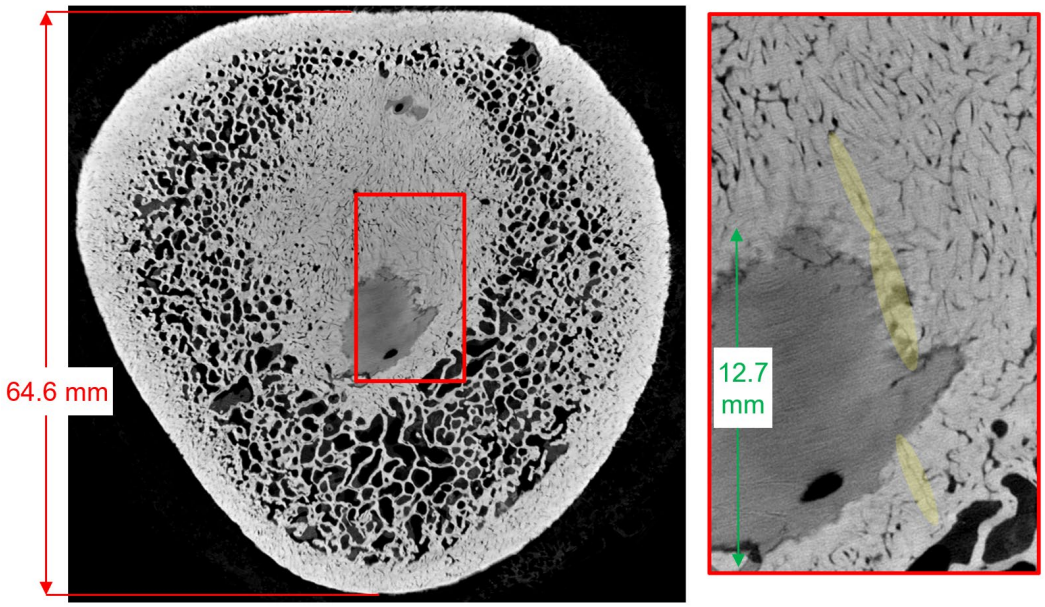


**Fig. 12 Post-experiment micro-CT image of HR02 full specimen (left) and zoomed in at loading point (right) with yellow highlighting of micro-fracture**

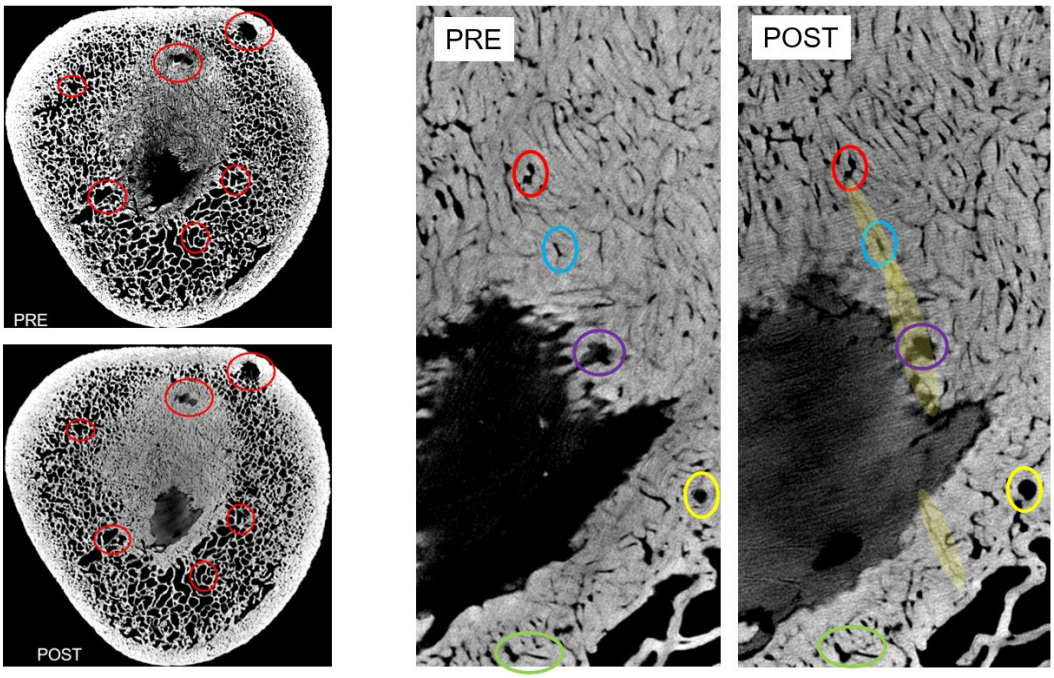


**Fig. 13 Micro-CT image comparison of pre- and posttest scan images for HR02 full specimen (left) and zoomed in at loading point (right) highlighting micro-fracture. Circular marks in pre- and posttest images highlight several features common to both images, indicating good registration between pre- and posttest micro-CT datasets.**

## 3.2 Quasi-static Rate Experiments

At quasi-static loading rate, macro-fracture was preceded by softening in the specimen mechanical response. Several experiments were conducted with the goal of reaching this softening and unloading the specimen after micro-fracture initiation but prior to macro-fracture; for these, either an edge fracture initiation was observed or no fracture was observed, and they were reloaded.

The quasi-static loading rate specimens exhibited brittle mechanical response similar to the high-rate specimens, with unstable macro-fracture growth, little to no permanent deformation, such as denting or cupping, around the loading point, and an approximately unchanged specimen height. The softening in the mechanical response does suggest some plastic behavior, although that could be accounted for by micro-fracture at the loading point or the edge.

In addition to obtaining the specimen load and corrected indenter displacement, full-field deformation data was obtained for the specimen inner surface using DIC. This allowed for creation of inner surface contours of several deformation profiles, including out-of-plane deformation along the loading axis (W) and principal strains (e1 and e2). These profiles were created for several discrete time steps during loading, where each profile represents the specimen deformation at that time (and therefore load and indenter displacement). These profiles are used to directly compare the experimental specimen deformation to those obtained during simulation, allowing another tool for validation of simulation predicted results. These profiles are shown in Appendix A. For brevity they are shown for specimen LR08 loading cycle 02 only; however, they are available for all of the specimens documented here.

### 3.2.1 Single Loading Experiments

Quasi-static loading rate experiment LR03 (ARL-2017-0019-LPAR) was loaded until fracture. Initially, the specimen load increased linearly; then the load began to soften and reached a plateau for approximately 25 s, where indenter displacement continued to increase while the specimen load remained constant. This was followed by unstable crack growth and immediate macro-fracture, with the primary fracture traveling between the loading point and specimen edge, shown in the posttest optical image (Fig. 14b). The location of fracture initiation could not be determined from the specimen DIC images, as initiation and growth happened entirely within the time between adjacent picture frames. Figure 14a shows load, corrected indenter displacement, and maximum inner surface BFD as a function of time for LR03. For LR03, the max load was 2.41 kN and the apparent stiffness was 1.99 kN/mm.

The posttest micro-CT scan of LR03 (Fig. 14c) showed that, in addition to the visible primary macro-fracture (referred to as Crack #1), two secondary fractures initiated at the loading point and partially propagated toward the edge (referred to as Cracks #2 and #3). Appendix B presents additional images of the fractures at different heights along the specimen thickness (y-axis).

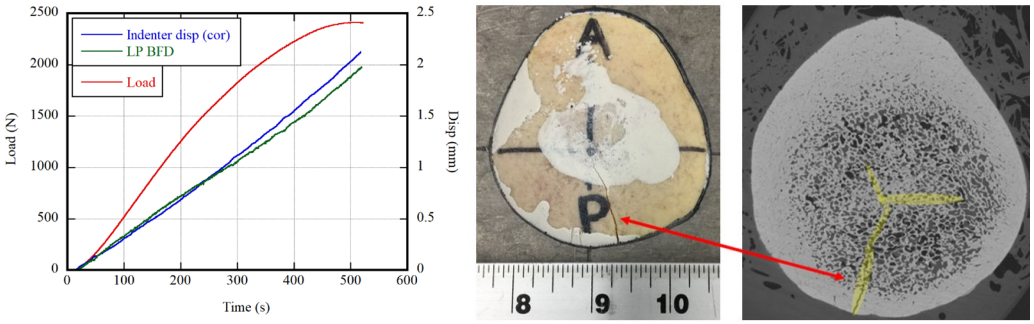


**Fig. 14 (a) Load, corrected indenter displacement, and max inner surface BFD vs. time for LR03, posttest; (b) visual and (c) micro-CT image indicating three fractures (yellow highlight)**

LR05 (ARL-2017-0015-LPAR) was loaded until reaching a load plateau; the load was removed after an arbitrarily chosen plateau duration of 10 s. No fracture under the loading point was observed in the posttest scan; however, fracture initiation was observed at the specimen edge (Fig. 15b, highlight). Figure 15a shows load, corrected indenter displacement, and maximum inner surface BFD as a function of time for LR05; the max load was 3.39 kN and the apparent stiffness was 2.16 kN/mm.

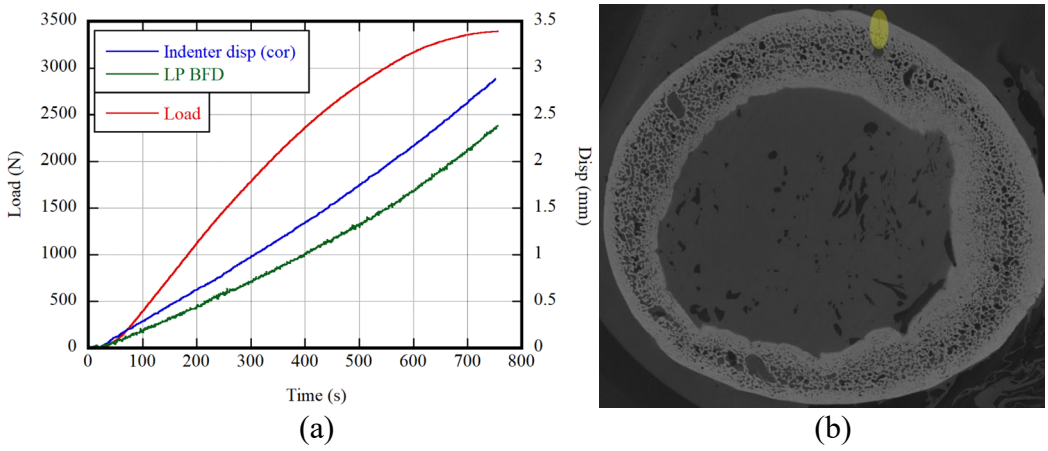


**Fig. 15 (a) Load, corrected indenter displacement, and max inner surface BFD vs. time for LR05; (b) posttest micro-CT image indicating edge fracture initiation (yellow highlight)**

LR06 (ARL-2017-0020-RPAR) was loaded and began to soften but did not reach a load plateau; the load increased to a max load of 2.06 kN, at which point macro-fracture occurred, traveling between the loading point and the specimen edge (Fig. 16b). The location of crack initiation could not be determined from the specimen DIC images; a high-speed camera was added to the experimental setup for subsequent experiments. Figure 16a shows load, corrected indenter displacement, and maximum inner surface BFD as a function of time. For LR06, the apparent stiffness was 2.051 kN/mm.

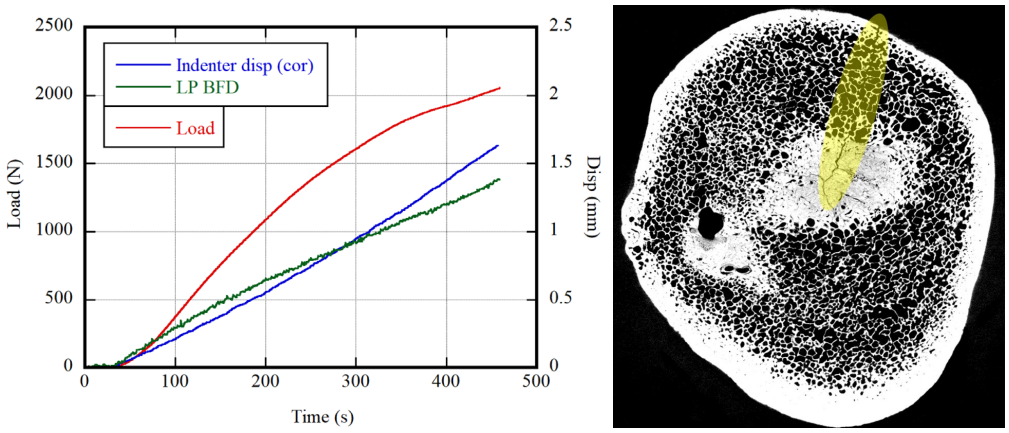


**Fig. 16 (a) Load, corrected indenter displacement, and max inner surface BFD vs. time for LR06; (b) posttest micro-CT image with macro-fracture highlighted**

For LR07 (ARL-2017-0014-FRONTAL), a high-speed camera (Photron SA5, 100K FPS) was added to observe the fracture initiation location, although it was not used for this specimen, which reached a load plateau of 3.76 kN, and after approximately 5 s, experienced a significant load decrease. This decrease was observed in real time, and the specimen was immediately unloaded to perform a posttest micro-CT scan. The posttest scan showed evidence of fracture initiation localized at the specimen edge traveling approximately 25% of the distance from edge to loading point (Fig. 17b). Figure 17a shows load, corrected indenter displacement, and maximum inner surface BFD as a function of time for LR07. The apparent stiffness for LR07 was 2.67 kN/mm.

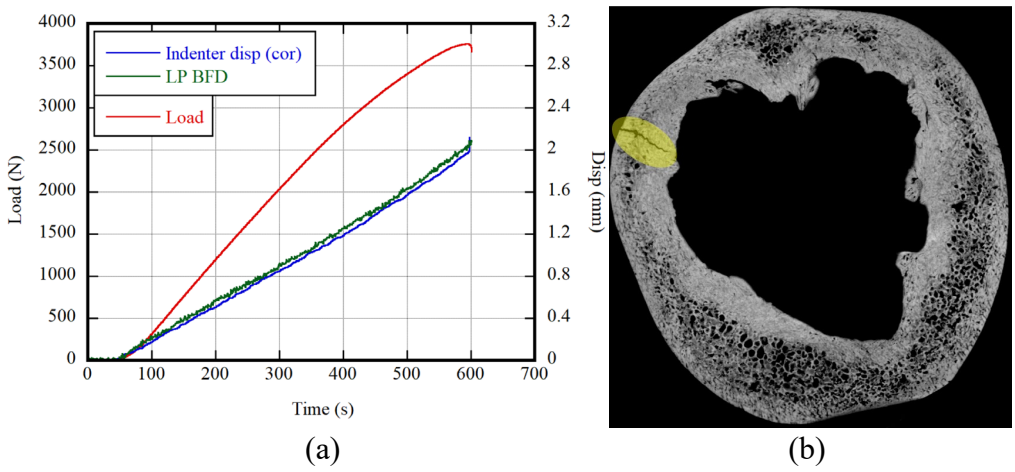


**Fig. 17 (a) Load, corrected indenter displacement, and max inner surface BFD vs. time for LR07; (b) posttest micro-CT image with edge fracture highlighted**

The final single loading specimen, LR10 (ARL-2017-0020-FRONTAL), had several changes made to the experimental setup in an attempt to obtain fracture initiation at the loading point. The backing plate was machined with a recess to constrain the specimen so that it was not free to expand outward during loading. The backing plate cutout edge was rounded off. An epoxy was used to pot the specimen and fill in the open pores in the cut surface, with the goal of reinforcing the specimen edge. These modifications to the experimental setup are shown schematically in Fig 18.

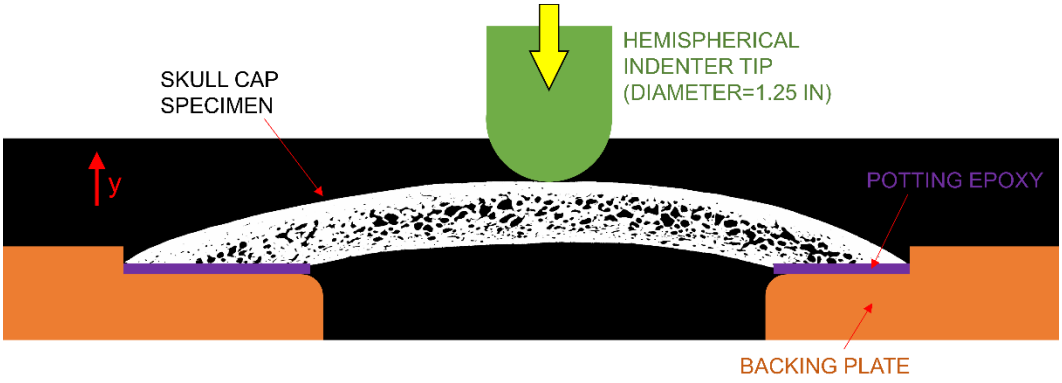


**Fig. 18 Quasi-static loading schematic for LR10. (The skullcap shown here was from LR03 and is used only for illustration.)**

During loading, LR10 reached a plateau load of 1.62 kN. The plateau was held for 20 s, and then the load was removed to allow for posttest micro-CT scan. The experimental setup changes seemed to have no effect; the posttest micro-CT scan indicated fracture initiation at the specimen edge (Fig. 19b). Figure 19a shows load, corrected indenter displacement, and maximum inner surface BFD as a function of time for LR10; the apparent stiffness was 2.30 kN/mm.

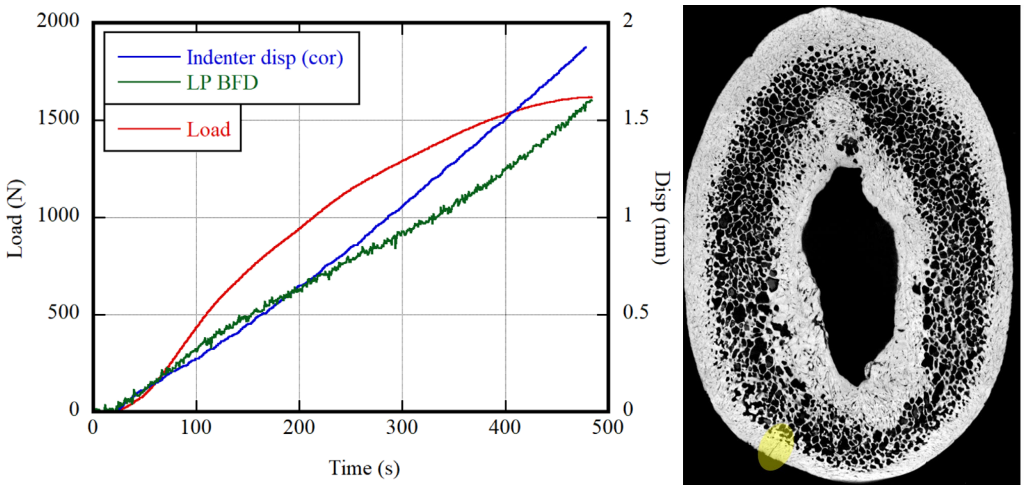


**Fig. 19 (a) Load, corrected indenter displacement, and max inner surface BFD vs. time for LR10; (b) posttest micro-CT image with edge fracture highlighted**

### 3.2.2 Multiple Loading Experiments

Two specimens were loaded multiple times: LR04 (ARL-2013-0007-LPAR) and LR08 (ARL-2017-0016-RPAR). LR04 was loaded for nine cycles and LR08 was loaded for two cycles.

LR04 was loaded to a series of increasing load levels. Once the target level was reached, the load was removed and the specimen was posttest micro-CT scanned. After the micro-CT scan, the process was repeated to a higher target load level. For LR04, the target load was reached with no load plateau and no evidence of softening during the initial six loading cycles. For these loading cycles, the target load levels were 1.56 kN (350 lb), 1.67 kN (375 lb), 1.78 kN (400 lb), 1.89 kN (425 lb), 2.00 kN (450 lb), and 2.11 kN (475 lb). The posttest micro-CT scans showed no evidence of fracture initiation following the first six loading cycles.

The target load level for the seventh cycle was 2.22 kN (500 lb). However, the specimen load reached a plateau at 2.11 kN, and the specimen was immediately unloaded after approximately 5 s. The posttest scan of loading cycle 07 showed a small crack at the inner surface just beneath the loading point (Fig. 20a). LR04 was subsequently reloaded two more times for a total of nine loading cycles. Figures 20b and 20c show the same crack in slightly different section planes. The crack appeared to grow along the specimen thickness in the posttest scans for these final two cycles. The specimen thickness for all three of these cycles was unchanged. The inability to see any other failures such as compressive (loss of load-carrying capacity under compression) in the diploe region in the posttest experimental images could be because the failed bone region may have sprung back

to the original shape after unloading (much like a sponge), which was not visible with the post-experiment micro-CT scans.

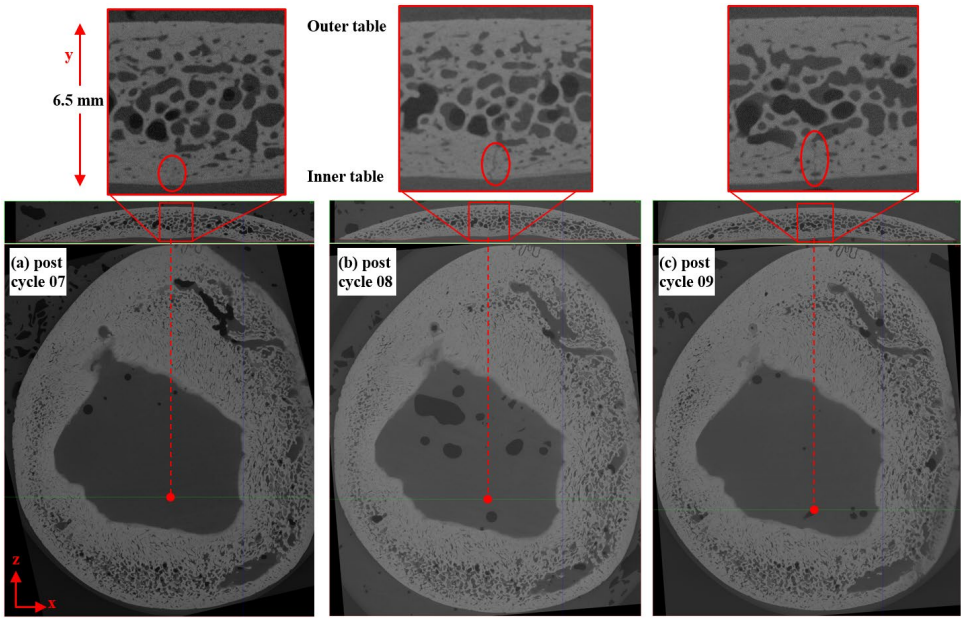


**Fig. 20 Posttest scan images of LR04 showing fracture initiation at inner surface after loading cycle 07 (a) and crack growth through the skull thickness after loading cycles (b) 08 and (c) 09. The images show the crack across slightly different section planes.**

The load history for all nine cycles of LR04 are shown in Fig. 21a, and load versus corrected displacement data is shown in Fig. 21b. The time between each cycle is an arbitrary value, chosen to maintain clarity; the actual time between loading cycles was over a week.

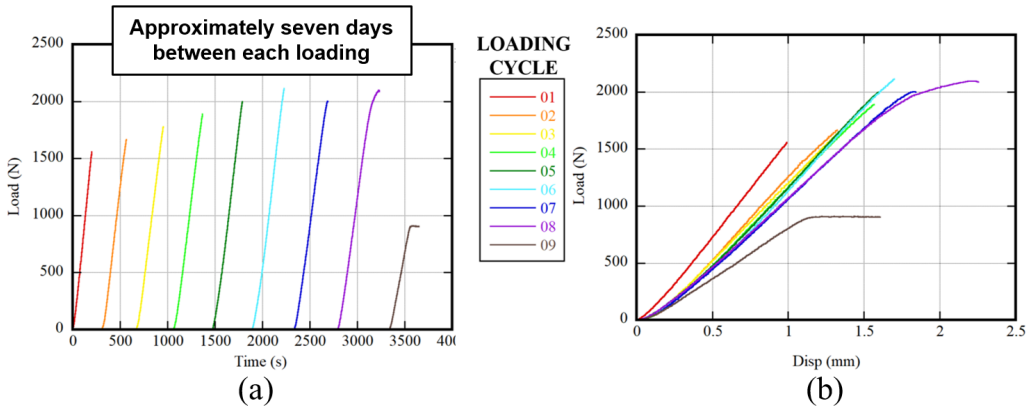


**Fig. 21 LR04 all loading cycles (a) load vs. time with arbitrary time spacing between loading cycles; (b) load vs. corrected indenter displacement**

The apparent stiffness as a function of loading cycle number for LR04 is shown in Fig. 22. The apparent stiffness for cycles 01–06 is approximately the same and decreases after fracture initiation and growth for cycles 07–09.

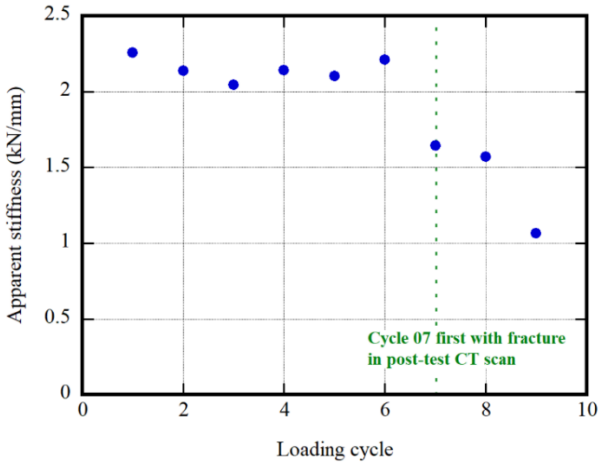


**Fig. 22 LR04 apparent stiffness as a function of loading cycle**

LR08 was loaded to plateau and held there for 15 s. The load was then immediately removed for posttest micro-CT scan, which showed no evidence of fracture initiation, either at the edge or under the loading point, as demonstrated in the micro-CT images provided in Appendix C. LR08 was then reloaded for a second cycle, where the load increased until the specimen experienced a sudden fracture with no evidence of load plateau. The low-resolution high-speed camera, which recorded the macro-fracture initiation and growth, indicated that macro-fracture initiated at the specimen edge and grew toward the loading point, taking approximately 150 μs (15 frames). The loading history for LR08 is shown in Fig. 23a, and the load versus corrected indenter displacement is shown in Fig. 23b for both loading cycles. The max load for loading cycles 01 and 02 were 3.20 and 2.84 kN, and the apparent stiffnesses were 2.06 and 1.92 kN/mm, respectively.

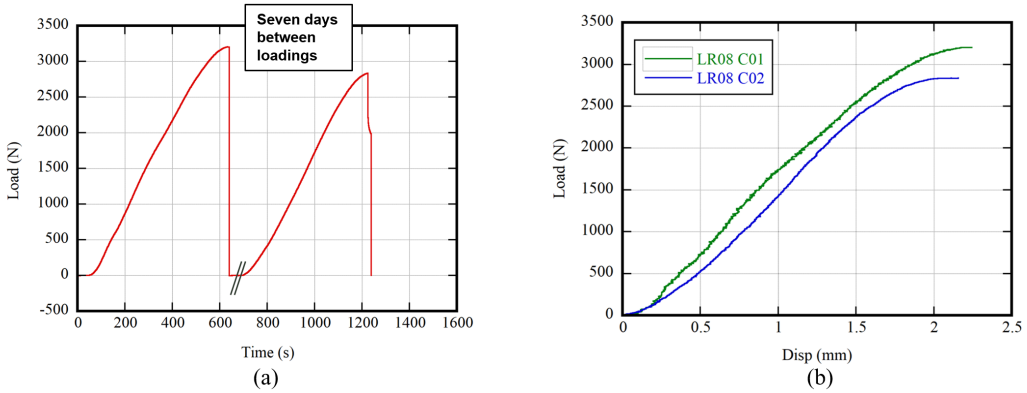


**Fig. 23 LR08 (a) load vs time and (b) load vs. corrected indenter displacement for both loading cycles**

## 3.3 Apparent Stiffness of Human Skull

Despite having different specimen microstructure, size, and geometry, the initial mechanical response at quasi-static loading rate of the skullcap specimens was similar. Figure 24 shows the load versus corrected indenter displacement for all of the single loading quasi-static experiments, as well as the first loading cycles for both multiple loading experiments.

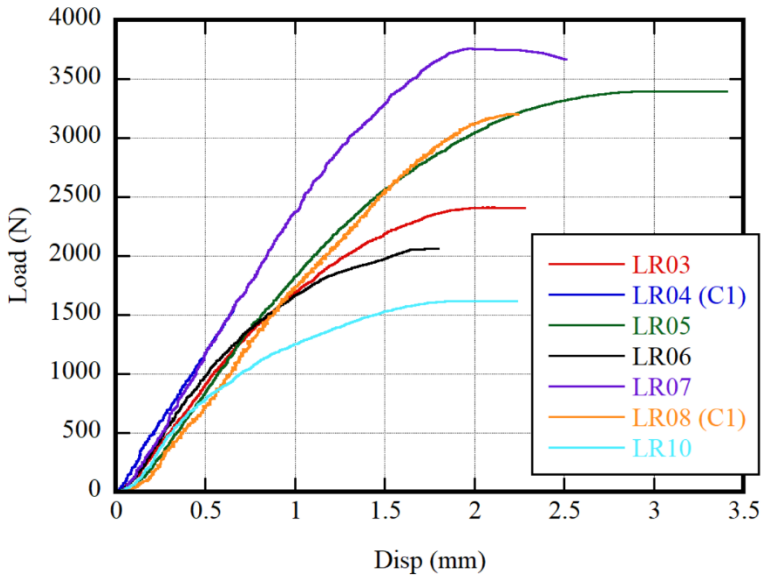


**Fig. 24 Load vs. corrected indenter displacement for all quasi-static results (first cycle only for multiple loading specimens)**

The apparent stiffness of the human skullcap specimens was much higher at the high loading rate relative to the quasi-static rate. This suggests that apparent stiffness is related to the loading rate, although the small number of high loading rate results limits the strength of this conclusion. The apparent stiffness as a function of loading rate is shown in Fig. 25, using only the first loading cycle for both multiple loading experiments.

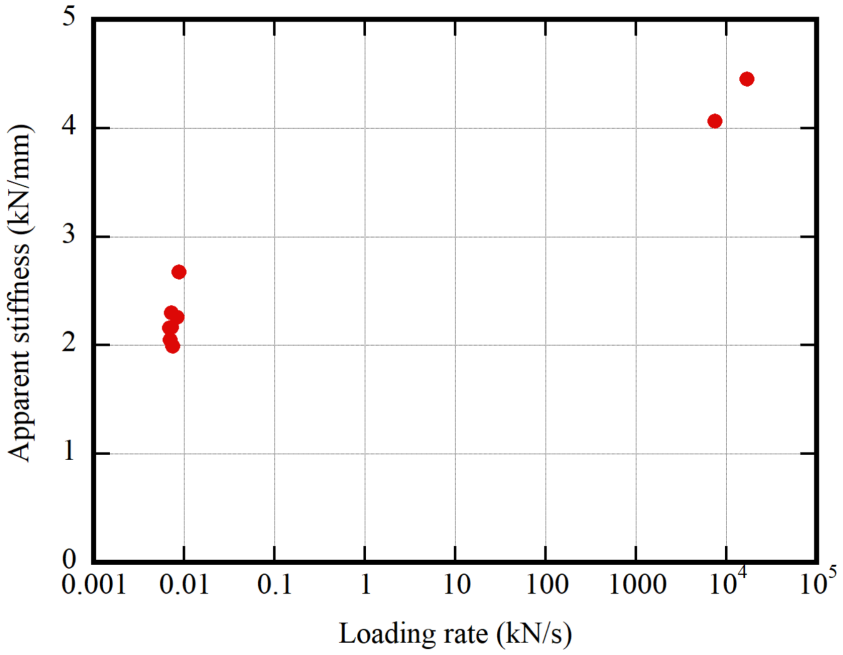


**Fig. 25 Apparent stiffness vs. loading rate for all skullcap specimens (first cycle only for multiple loading specimens)**

## 4. Discussion and Limitations

This study characterized the mechanical response of human skull to blunt indentation loading as a function of loading rate. Results obtained from this study have been used to implement skull fracture mechanisms into finite element models to improve simulation accuracy of predicting skull fracture initiation (Alexander et al. 2020b; Weerasooriya and Alexander 2020). Computational limitations restrict the use of detailed structure, such as pore structure, that could be accurately represented in a full head and head protection model. As a result, in these works solid elements successfully represented areas of the skull that are porous with equivalent moduli and failure stresses based on the local microstructural porosity, thus reducing the complexity of the finite element computation. Therefore, it is important to utilize microstructurally inspired material models for these elements, which intrinsically account for the porous heterogeneous nature of the skull, to improve the biofidelity of the model over simply using parameters derived for homogenized bone. Thompson et al. (2016) demonstrated that modeling the Gottingen minipig skull with a 10-layer system, using experimentally determined material properties for each layer, made a significant difference on the peak pressure experienced in the brain during simulations of head impact. However, it may not be feasible to incorporate multilayer models in large-scale simulations; therefore, it is important to have models that are able to represent the skull mechanical response with its local structure.

For the experiments documented here, the specimens experienced load increase, followed by a brief softening and load plateau in the quasi-static rate experiments, and then macro-fracture initiation. This is in contrast with the behavior exhibited by the human skull in uniaxial compression (Alexander et al. 2020a), which demonstrated a three-part load-displacement response. Fracture for the skullcap during indentation loading was frequently localized to the inner table, while in compression the skull exhibited fracture initiation, significant damage, and failure localized almost exclusively in the diploe. These differences in mechanical response and fracture are due to the difference in stress state applied to the skull in the two different experimental studies.

The mechanical characterization reported here was performed on a limited number of human skulls. The skulls were acquired from 70- to 85-year-old PMHS, who are not representative of the military-age population. Therefore, it is unknown whether these results are representative of the deformation and fracture behavior of human skull found in Army-relevant aged people.

## 4.1 Fracture Initiation at Specimen Edge

During loading of the skull in BHBT full head experiments, skull fracture is presumed to initiate at the loading point and propagate outward, as posttest autopsy of the head showed fracture or fractures with the impact point centered, not travelling to a free surface but arrested some distance from the loading point. However, in the experiments reported here, macro-fracture frequently appears to have initiated at the specimen edge and propagated toward the loading point. Micro-fracture localized at or near the loading point was observed in several specimens (HR02, LR03, LR04). It is possible that micro-fracture, which was not able to be recognized as separate from the microstructure, occurred at the loading point in other specimens. It was difficult to distinguish the porous structure of the skull from the micro-fracture even with direct comparison of the registered pre- and posttest micro-CT scan datasets.

Nonetheless, the primary macro-fracture initiation location was at the specimen edge; there are several possible factors contributing to localization of fracture initiation at the specimen edge for this geometry. The distance between the loading point and the specimen edge is not far (approximately 25–50 mm), whereas in full head/skull experiments, the distance between the loading point and a free surface of the skull is much greater. Several full skull BHBT experiments saw fracture between the loading point and an eye socket, which is the nearest free surface for an impact to the frontal or parietal bones. Defects may have been created in the skullcap specimen microstructure at the specimen edge during fabrication, which

may have created stress concentrations that are not present in a full, uncut skull. Finally, the geometry of these specimens caused the specimen edge to be very thin, whereas in a complete skull, at the same location relative to the loading point, the skull would be full thickness. It is likely that some combination of these artifacts lowered the fracture toughness at the skullcap specimen edge, creating conditions conducive to fracture initiation at the skullcap edge that would not exist in a full skull during BHBT.

These artifacts may be a contributing factor to the high variability observed in the specimen fracture (max) load, in addition to the local microstructural variations. Fracture in brittle materials is often defect driven. With the possibility here of defect creation in the fabrication process, this could artificially lower the fracture toughness in some specimens. The skullcap apparent stiffness, which is less likely to be dependent on specimen defects and more dependent on geometry, microstructure, and material properties, was approximately constant at each loading rate.

Minimization of fracture initiation at the specimen edge may be accomplished by using larger specimens, with a longer distance between the loading point and specimen edge. However, the skullcap specimens used here are approximately the size of each skull bone (frontal or parietal) and are fabricated from the upper skull (see Fig. 1), which is relevant to head protection research. Increasing the skullcap size would involve making specimens that have large curvature where the skull top meets the more vertical skull side surface around the upper ear. In addition, larger skullcap specimens would necessarily include skull bone sutures, complicating the simulation of the skull response. It may be possible to fabricate skullcap specimens without a thin specimen edge, by sanding or grinding the specimen edge toward the loading point until the remaining specimen edge has a greater thickness (Fig. 26). This smaller specimen could also be regularly shaped, such as square or circular, aiding in obtaining a tight fit with the backing plate for in-plane constraint, as that portion of the skullcap would be as part of a skull.


**Fig. 26 Illustration of skullcap specimen with thin specimen edge removed. The skullcap shown here is from LR03.**

## 4.2 Rate Limitations

The high-rate indenter tip velocity and loading rates used here are lower than typical BHBT events; the apparent stiffness and fracture loads reported here for the high loading rate may not be representative of the skull mechanical behavior at BHBT events. It was not possible to control specimen deformation at high loading rate and stop loading just at the onset of fracture initiation indication in real time as it was at the quasi-static loading rate, so there may be other fracture mechanisms occurring at high loading rate that were not observed here.

## 4.3 Machine Load Train Compliance and Indenter Tip Deformation

The raw indenter tip displacement was measured two ways: using the test internal extensometer of the test machine and optical measurement of the indenter displacement using 2-D DIC. Frequently in mechanical testing, there is compliance of the loading train components (fixtures, load cell, etc.) as they deform slightly, causing error in the machine extensometer measurement. Here, DIC was used to measure the actual indenter displacement to eliminate the error due to the machine compliance. However, for this experimental setup, the two measures were found to be identical.

It was assumed that the indenter tip does not deform during loading. This assumption was verified by quantification of indenter tip deformation during loading using the DIC data from the indenter tip displacement.

## 4.4 Effect of Irradiation Absorption on Bone

The skullcap bone specimens used here for blunt indentation loading experiments were first scanned using micro-CT to understand their structure and orientation. The micro-CT process causes the bone to absorb a radiation dosage during exposure to the X-ray beam in the micro-CT. There are studies that suggest irradiation exposure may alter the mechanical properties of bone due to degradative effects on the collagen (Anderson et al. 1992; Hamer et al. 1996; Currey et al. 1997; Cornu et al. 2000; Vastel et al. 2004; Barth et al. 2010, 2011). Specifically, irradiation causes radiolysis of water, which can induce collagen cross-linking, decreasing plasticity and increasing brittleness (Colwell et al. 1996). Most studies report a significant effect from irradiation dosage on the plastic collagenic material properties with negligible effect on elastic properties. Barth et al. (2010) reported a significant reduction in bending strength, plasticity, and fracture toughness in human cortical bone with increasing irradiation dosage, but no effect on bending stiffness. Currey et al. (1997) reported significant decreases in bending strength, work to fracture,

and impact energy absorption with increasing irradiation dosage in human bone; however, the elastic modulus was unchanged. These studies have concerned the X-ray exposure of bone in high-power X-ray equipment, such as a synchrotron, with irradiation dosages of approximately $10^2$–$10^3$ kGy. However, the irradiation dosages that bone specimens receive in low-power micro-CT scanning (approximately $10^{-1}$–$10^0$ kGy) are typically well below the dosages shown to cause degradation of plastic mechanical properties in human bone (Gunnarsson et al. 2018).

## 5. Conclusions

The mechanical response of the human skull to blunt indentation loading was quantified as a function of loading rate using skullcap scale specimens. Micro-CT imaging with a voxel resolution of approximately 25 μm was used to quantify the skull structure prior to loading. The micro-CT imaging was repeated after unloading to understand the effect of loading on the structure of the specimen. Damage initiation and subsequent propagation were identified by observing micro- and macro cracks, and comparing the pre- and posttest images. In-situ optical DIC methods were used to measure the 3-D deformation of the skull during loading.

The skull exhibited brittle material behavior, with initial deformation followed by initiation of fracture. There was little to no permanent deformation, such as denting or cupping, around the loading point region, and the specimen height was approximately unchanged. Most specimens experienced macro-fracture initiation at the specimen edge, although that is likely an artifact of specimen geometry and fabrication. Micro-fracture initiation was observed in several specimens in the inner table just at or near the loading point.

The apparent stiffness of human skull was measured and appears to be dependent on loading rate, with increasing rate corresponding to increasing stiffness. The apparent stiffness was relatively constant for skull specimens for repeated cycles of load–unload–scan to incrementally higher load levels until initiation of the fracture process. The experimental results reported here will allow researchers to incorporate fracture initiation mechanisms into computer models and subsequent validation of these models, improving the injury predictive capability through computer simulations of BHBT events.

## 6. References


Alexander SL, Gunnarsson CA, Weerasooriya T. Influence of the mesostructure on the compressive mechanical response of adolescent porcine cranial bone. Journal of the Mechanical Behavior of Biomedical Materials. 2019a;96:96–107.

Alexander SL, Rafaels K, Gunnarsson CA, Weerasooriya T. Structural analysis of the frontal and parietal bones of the human skull. Journal of the Mechanical Behavior of Biomedical Materials. 2019b;90:689–701.

Alexander SL, Gunnarsson CA, Rafaels K, Weerasooriya T. Multiscale response of the human skull to quasi-static compression. Journal of the Mechanical Behavior of Biomedical Materials. 2020a;102:103492.

Alexander SL, McKee PJ, Weerasooriya T. Micro-CT-based three-layer finite element model for quasi-static human skull indentation. DEVCOM Army Research Laboratory (US); 2020b May. Report No.: ARL-TR-8962.

Anderson M, Keyak J, Skinner H. Compressive mechanical properties of human cancellous bone after gamma irradiation. J Bone Joint Surg Am. 1992;74(5):747–752.

Barth H, Launey M, MacDowell A, Ager J, Ritchie R. On the effect of X-ray irradiation on the deformation and fracture behavior of human cortical bone. Bone. 2010;46(6):1475–1485.

Barth H, Zimmermann E, Schaible E, Tang S, Alliston T, Ritchie R. Characterization of the effects of X-ray irradiation on the hierarchical structure and mechanical properties of human cortical bone. Biomaterials. 2011;32(34):8892–8904.

Baumer TG, Powell BJ, Fenton TW, Haut RC. Age dependent mechanical properties of the infant porcine parietal bone and a correlation to the human. Journal of Biomechanical Engineering. 2009;131(11):111006.

Boruah S, Henderson K, Subit D, Salzar R, Shender B, Paskoff G. Response of human skull bone to dynamic compressive loading. Proceedings of the International Research Council on Biomechanics of Injury (IRCOBI) Conference; 2013 Sep 11–13; Gothenburg, Sweden. Vol. 13; p. 497.

Boruah S, Subit DL, Paskoff GR, Shender BS, Crandall JR, Salzar RS. Influence of bone microstructure on the mechanical properties of skull cortical bone—a combined experimental and computational approach. Journal of the Mechanical Behavior of Biomedical Materials. 2017 Jan 1;65:688–704.

Brown AD, Rafaels K, Weerasooriya T. Shear behavior of human skull bones. Journal of the Mechanical Behavior of Biomedical Materials. 2021;115: 104343.

Bullock MR, Chesnut R, Ghajar J, Gordon D, Hartl R, Newell DW, Servadei F, Walters BC, Wilberger J. Surgical management of depressed cranial fractures. Neurosurgery. 2006 Mar 1;58(suppl_3):S2-56.

Colwell A, Hamer A, Blumsohn A, Eastell R. To determine the effects of ultraviolet light, natural light and ionizing radiation on pyridinium cross-links in bone and urine using high-performance liquid chromatography. European Journal of Clinical Investigation. 1996;26(12):1107–1114.

Cornu O, Banse X, Docquier P, Luyckx S, Delloye C. Effect of freeze-drying and gamma irradiation on the mechanical properties of human cancellous bone. Journal of Orthopaedic Research. 2000;18(3):426–431.

Currey J, Foreman J, Laketic I, Mitchell J, Pegg D, Reilly G. Effects of ionizing radiation on the mechanical properties of human bone. J Orthop Res. 1997;15(1):111–117.

Delille R, Lesueur D, Potier P, Drazetic P, Markiewicz E. Experimental study of the bone behaviour of the human skull bone for the development of a physical head model. International Journal of Crashworthiness. 2007 Aug 21;12(2):101–8.

Dempster WT. Correlation of types of cortical grain structure with architectural features of the human skull. American Journal of Anatomy. 1967;120(1):7–31.

Gibson LJ, Ashby MF. Cellular solids: structure and properties. Cambridge University Press; 1997.

Gunnarsson CA, Alexander SL, Weerasooriya T. Morphological and mechanical characterization of adolescent Yucatan miniature porcine skull. Army Research Laboratory (US); 2018 Sep. Report No.: ARL-TR-8489.

Gunnarsson CA, Alexander SL, Weerasooriya T. Bending response of human skull as a function of loading rate and loading geometry. Army Research Laboratory (US); Forthcoming 2021.

Hamer A, Strachan J, Black M, Ibbotson C, Stockley I, Elson R. Biomechanical properties of cortical allograft bone using a new method of bone strength measurement – a comparison of fresh, fresh-frozen and irradiated bone. Journal of Bone Joint Surgery. Britain Volume. 1996;78(3):363–368.

Hisley DM, Gurganus JC, Drysdale AW. Experimental methodology using digital image correlation to assess ballistic helmet blunt trauma. Journal of Applied Mechanics. 2011 Sep 1;78(5).

Hubbard RP. Flexure of layered cranial bone. Journal of Biomechanics. 1971;4(4):251–263.

Ivancik J, Gurganus JC, Pizzolato KM, Horsmon MS, Mermagen WH. Behind Helmet Blunt Trauma (BHBT) Pilot Program Methodology. Army Research Laboratory (US), 2018 Sep. Report No.: ARL-TR-8518.

Margulies SS, Thibault KL. Infant skull and suture properties: measurements and implications for mechanisms of pediatric brain injury. Journal of Biomechanical Engineering. 2000;122(4):364–371.

Matheis EA, Eidsmore AE, Rafaels KA. Ballistic Factors of Behind Helmet Blunt Trauma Skull Fracture. In: 31st International Symposium on Ballistics; 2019.

McElhaney JH, Fogle JL, Melvin JW, Haynes RR, Roberts VL, Alem NM. Mechanical properties of cranial bone. Journal of Biomechanics. 1970;3(5):495–511.

Meaney DF, Morrison B, Bass CD. The mechanics of traumatic brain injury: a review of what we know and what we need to know for reducing its societal burden. Journal of Biomechanical Engineering. 2014;136(2).

Motherway JA, Verschueren P, Van der Perre G, Vander Sloten J, Gilchrist MD. The mechanical properties of cranial bone: the effect of loading rate and cranial sampling position. Journal of Biomechanics. 2009;42(13):2129–2135.

Multi-agency Leadership Panel (CDC, NIH, DoD, and VA). Report to Congress on traumatic brain injury in the United States: understanding the public health problem among current and former military personnel. Centers for Disease Control and Prevention (CDC), the National Institutes of Health (NIH), the Department of Defense (DOD), and the Department of Veterans Affairs (VA); 2013.

Nemat-Nasser S, Isaacs JB, Starrett JE. Hopkinson techniques for dynamic recovery experiments. Proceedings of the Royal Society of London. Series A: Mathematical and Physical Sciences. 1991 Nov 8;435(1894):371–91.

Peterson J, Dechow PC. Material properties of the human cranial vault and zygoma. The Anatomical Record Part A: Discoveries in Molecular, Cellular, and Evolutionary Biology. 2003;274(1):785–797.

Rahmoun J, Auperrin A, Delille R, Naceur H, Drazetic P. Characterization and micromechanical modeling of the human cranial bone elastic properties. Mechanics Research Communications. 2014;60:7–14.

Ritchie RO, Kinney JH, Kruzic JJ, Nalla RK. A fracture mechanics and mechanistic approach to the failure of cortical bone. Fatigue & Fracture of Engineering Materials & Structures. 2005 Apr;28(4):345–71.

Sanborn B, Gunnarsson CA, Foster M, Weerasooriya T. Quantitative visualization of human cortical bone mechanical response: studies on the anisotropic compressive response and fracture behavior as a function of loading rate. Experimental Mechanics. 2016 Jan 1;56(1):81–95.

Thompson KA, Sokolow AC, Ivancik J, Zhang TG, Mermagen WH, Satapathy SS. A sensitivity study of the porcine head subjected to bump impact. In: ASME 2016 International Mechanical Engineering Congress and Exposition, American Society of Mechanical Engineers; 2016 Nov 11–17; Phoenix, AZ. pp. V003T04A047-V003T04A047.

Tseng WC, Shih HM, Su YC, Chen HW, Hsiao KY, Chen IC. The association between skull bone fractures and outcomes in patients with severe traumatic brain injury. Journal of Trauma and Acute Care Surgery. 2011 Dec 1;71(6):1611-4.

Vastel L, Meunier A, Siney H, Sedel L, Courpied J. Effect of different sterilization processing methods on the mechanical properties of human cancellous bone allografts. Biomaterials. 2004;25(11):2105–2110.

Verschueren P, Delye H, Berckmans D, Verpoest I, Goffin J, Vander Sloten J, Van der Perre G. Analysis of fracture characteristics of cranial bone for FE modelling. InIRCOBI Conference 2006.

Weerasooriya T, Alexander SL. Micro-CT-based hybrid experimental-modeling-computational concept: determine skull fracture. DEVCOM Army Research Laboratory (US); 2020 Dec. Report No.: ARL-TR-9125.

Weerasooriya T, Sanborn B, Gunnarsson CA, Foster M. Orientation dependent compressive response of human femoral cortical bone as a function of strain rate. Journal of Dynamic Behavior of Materials. 2016 Mar 1;2(1):74–90.

Wood JL. Dynamic response of human cranial bone. Journal of Biomechanics. 1971 Jan 1;4(1):1–12.

# Appendix A. Full-field Deformation Contours for LR08 (ARL-2017-0016-RPAR)*

* This specimen was the subject in the simulation study of Weerasooriya and Alexander (Micro-CT-based hybrid experimental-modeling-computational concept: determine skull fracture. DEVCOM Army Research Laboratory (US); 2020 Dec. Report No.: ARL-TR-9125).

The following two figures show full-field deformation profiles for out-of-plane deformation (W) in A.1 and principal strain (e1) in A.2 for LR08 during loading cycle 02 at several discrete time points. This was the skullcap specimen used in the simulation study of Weerasooriya and Alexander.[1] Those time points are represented by the red dots in the load versus raw indenter displacement graph shown in the upper left for each profile series. Profile E is for the image just before macro-fracture occurred, and profile F is for the image just after macro-fracture occurred.

## A.1 BFD along Loading Axis

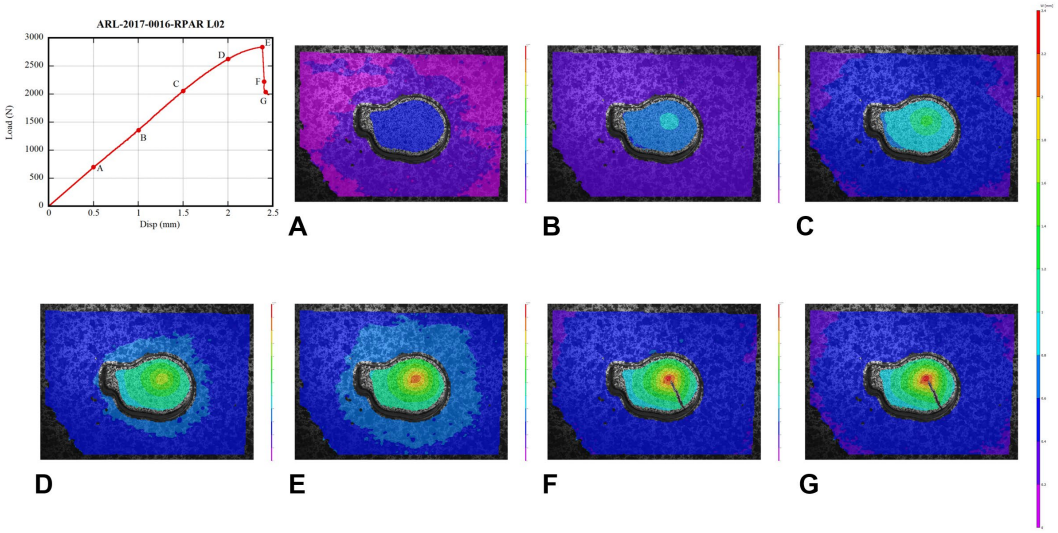


**Fig. A-1 Full-field BFD profiles for several discrete time points during loading for LR08 loading cycle 02. The letter label under each profile cooresponds to the time of letter label at that load in the load vs. time graph.**

[1] Weerasooriya T, Alexander SL. Micro-CT-based hybrid experimental-modeling-computational concept: determine skull fracture. DEVCOM Army Research Laboratory (US); 2020 Dec. Report No.: ARL-TR-9125.

## A.2 Principal Strain (e1)

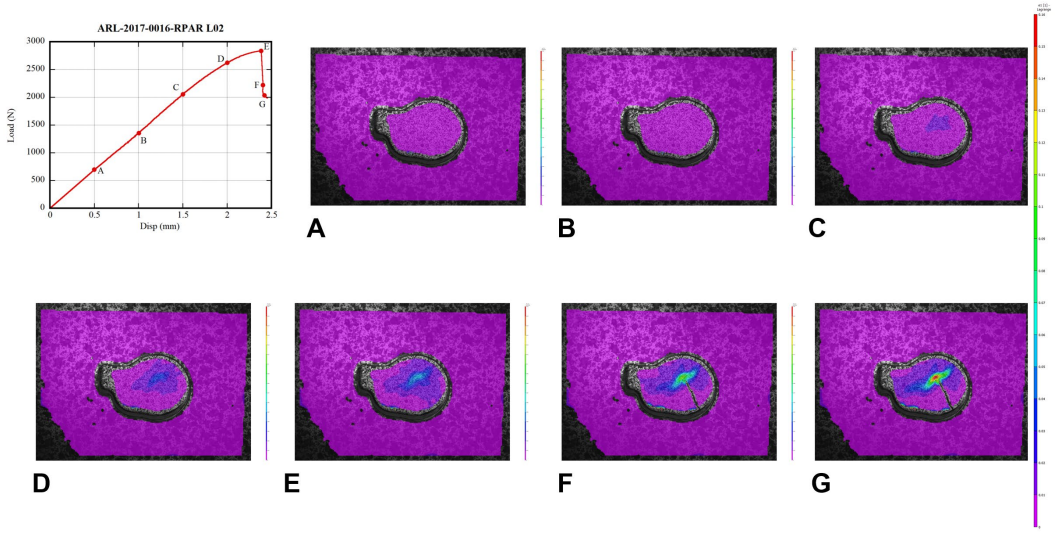


**Fig. A-2 Full-field principal strain (e1) profiles for several discrete time points during loading for LR08 loading cycle 02. The letter label under each profile cooresponds to the time of letter label at that load in the load vs. time graph.**

# Appendix B. Fracture of LR03 (ARL-2017-0019-LPAR)

Specimen LR03 (ARL-2017-0019-LPAR) was loaded once. The specimen had one macro-fracture, referred to here as Crack #1. This crack went through the entire thickness (inner table through outer table) and traveled between the loading point and specimen edge. It was observable visually without tomography or magnification (Fig. 14b).

There were also two secondary crack systems observed in the posttest microcomputed tomography (micro-CT) images. These are referred to here as Cracks #2 and #3. These cracks had a common point under the indenter and extended toward the specimen edge. Figure B-1 shows all three crack systems in the inner table under the indenter in the cross-section image (Fig. B-1b) and in the cross-section image enlargement of the area under the indenter (Fig. B-1c). The *y*-value (thickness value) of the cross section (Fig. B-1b) is indicated by the blue line in the through-thickness cross section (Fig. B-1a). This *y*-value indicates that the cross section (Fig. B-1b) cuts through the region under the loading point in the inner table. The cross-section image (Fig. B-1b) indicates that neither of the secondary cracks extended completely to the specimen edge. In addition, these cracks were not visible in the micro-CT images of the outer table (not shown), indicating that they did not go through the entire thickness of the skull.

Figure B-2 shows the cross section (Fig. B-2b) at a higher *y*-value compared to Fig. B-1b, located in the diploe, of the through-thickness cross section (Fig. B-2a). Figure B-2c is the cross-section enlargement of the area under the indenter and illustrates that, in the diploe under the indenter, Cracks #2 and #3 manifested as diffuse cracking rather than as clearly identifiable crack systems.

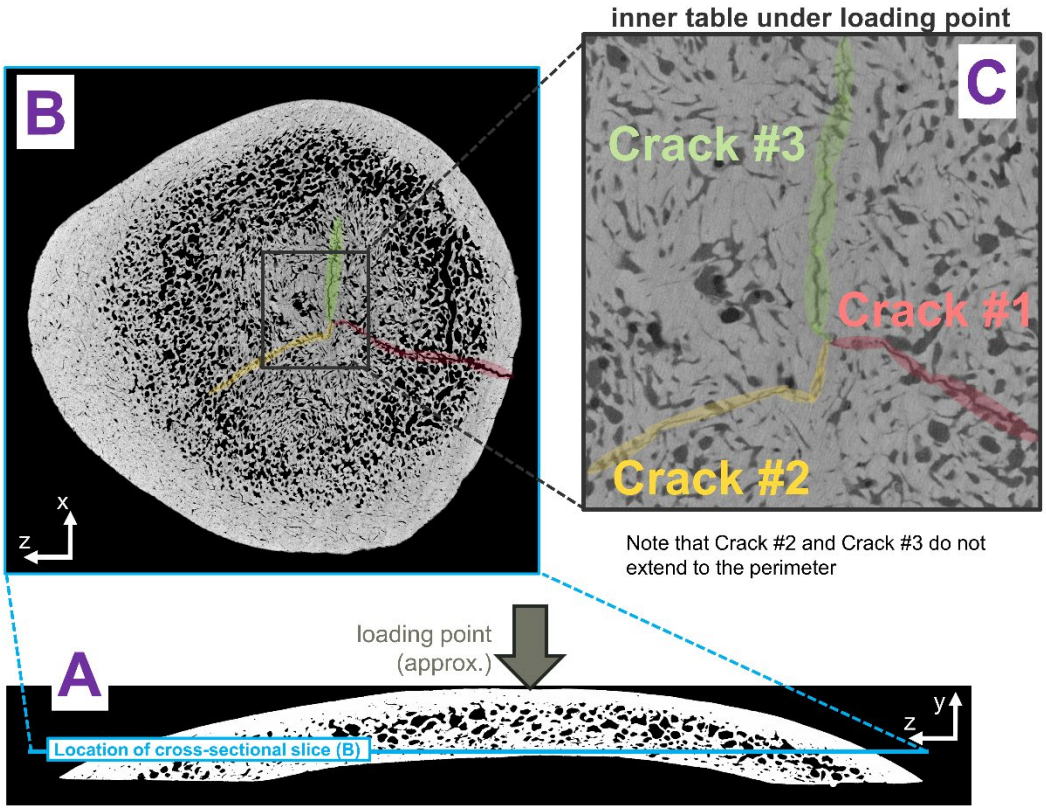


**Fig. B-1 Cracks in the inner table near the loading point for LR03. (A) The through-thickness cross section with outer surface on top and inner surface on bottom. (B) Cross-sectional view. The *y*-value (thickness value) of the cross section is indicated by the blue line in (A). This blue line indicates that the cross section cuts through the region under the loading point in the inner table. (C) Enlargement of the cross-sectional view in the area under the impactor.**

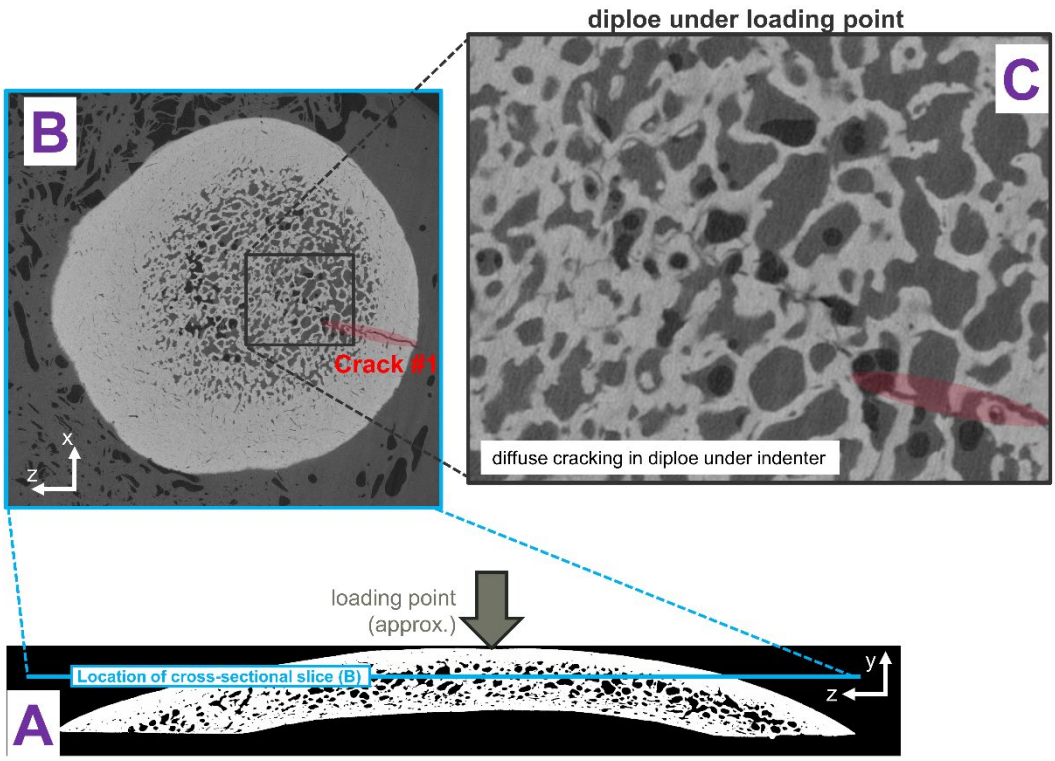


**Fig. B-2 Cracks in the diploe near the loading point for LR03. (A) The through-thickness cross section with outer surface on top and inner surface on bottom. (B) Cross-sectional view. The *y*-value (thickness value) of the cross section is indicated by the blue line in (A). This blue line indicates that the cross section cuts through the region under the loading point in the diploe. (C) Enlargement of the cross-sectional view in the area under the impactor.**

# Appendix C. Fracture of LR08 (ARL-2017-0016-RPAR)*

* This specimen was used in the simulation study of Weerasooriya and Alexander (Micro-CT-based hybrid experimental-modeling-computational concept: determine skull fracture. DEVCOM Army Research Laboratory (US); 2020 Dec. Report No.: ARL-TR-9125).

Specimen LR08 (ARL-2017-0016-RPAR) was a multiple loading experiment, loaded for two cycles. This was the skullcap specimen used in the simulation study by Weerasooriya and Alexander documenting the incorporation of skull fracture mechanisms into computational modeling.[1] The specimen was microcomputed tomography (micro-CT) scanned pretest (prior to loading), after the first loading cycle, and after the second loading cycle. Figures C-1 though C-3 compare images of specimen LR08 pretest, after the first loading cycle, and after the second loading cycle. They indicate that fracture observed after the second loading cycle was not observed after the first loading cycle or in the specimen pretest.

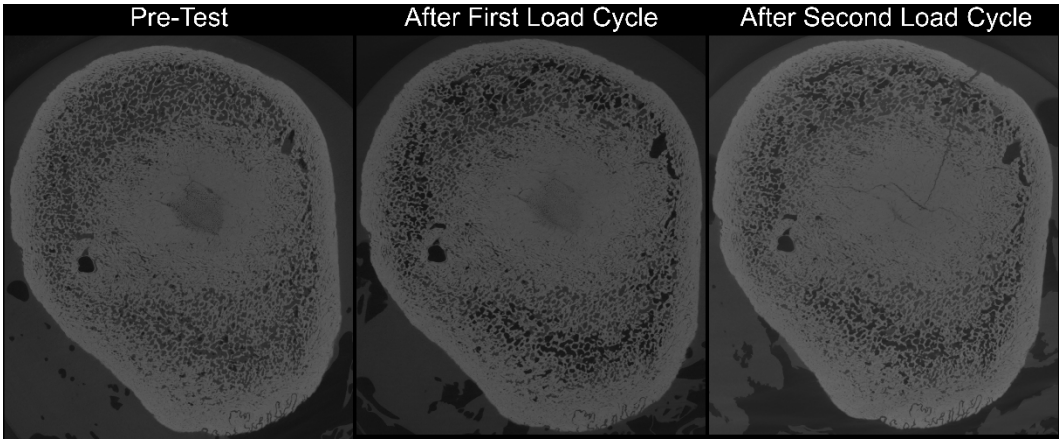


**Fig. C-1 Comparison of cross-section micro-CT images for LR08. Fracture is observed after the second loading cycle and is not observed pretest or after the first loading cycle.**

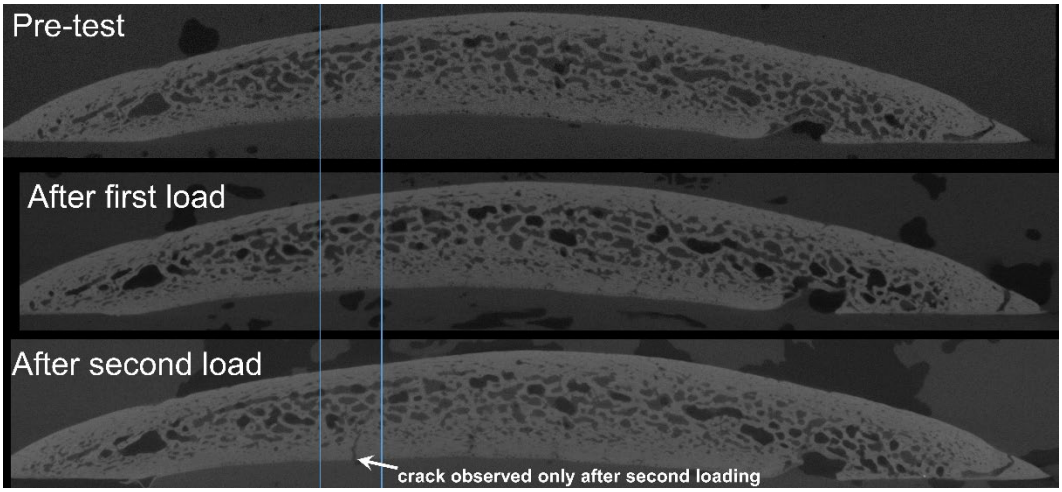


**Fig. C-2 Comparison of through-thickness micro-CT images. Fracture is observed after the second loading cycle and is not observed pretest or after the first loading cycle.**

[1] Weerasooriya T, Alexander SL. Micro-CT-based hybrid experimental-modeling-computational concept: determine skull fracture. DEVCOM Army Research Laboratory (US); 2020 Dec. Report No.: ARL-TR-9125.

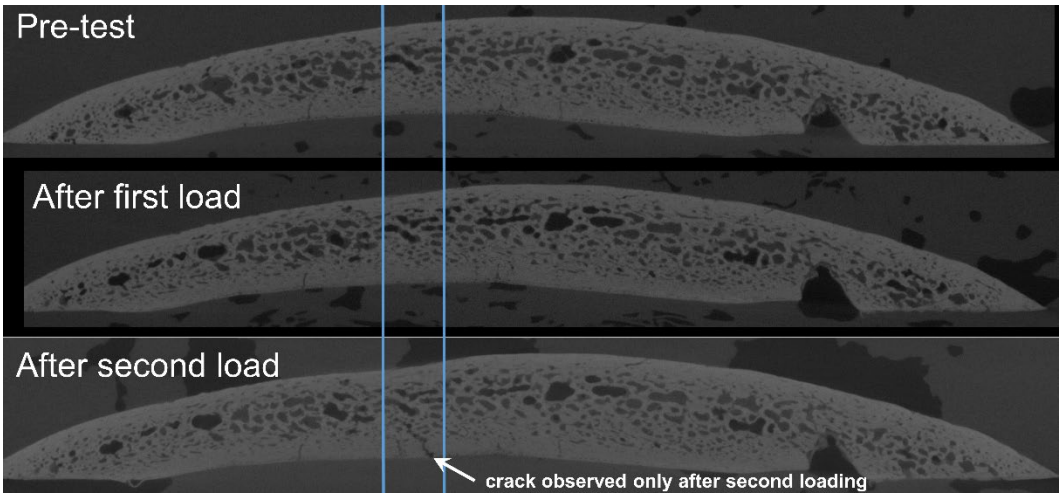


**Fig. C-3 Additional comparison of through-thickness micro-CT images. Fracture is observed after the second loading cycle and is not observed pretest or after the first loading cycle.**

## List of Symbols, Abbreviations, and Acronyms

| | |
|---|---|
| 2-D | two-dimensional |
| 3-D | three-dimensional |
| ARL | Army Research Laboratory |
| BFD | backface deformation |
| BHBT | behind-helmet blunt trauma |
| DEVCOM | US Army Combat Capabilities Development Command |
| CT | computed tomography |
| DIC | digital image correlation |
| fps | frames per second |
| HBSS | Hank's Balanced Salt Solution |
| IT | inner table |
| MD | mid-dipole |
| micro-CT | microcomputed tomography |
| OT | outer table |
| PMHS | postmortem human subjects |
| SHPB | split Hopkinson pressure bar |
| TBI | traumatic brain injury |

1 (PDF) DEFENSE TECHNICAL INFORMATION CTR
DTIC OCA

1 (PDF) DEVCOM ARL
FCDD RLD DCI
TECH LIB

1 (PDF) DEVCOM ARL ARO
FCDD RLR
D STEPP

11 (PDF) CCDC NATICK SOLDIER SYSTEMS CTR
M G CARBONI
D COLANTO
R DILLALLA
B FASEL
J FONTECCHIO
B KIMBALL
J KIREJCZYK
J PARKER
M MAFEO
M MARKEY
D PHELPS

3 (PDF) PROG EXECUTIVE OFC SOLDIER
J HOPPING
J MULLENIX
D OTTERSON

1 (PDF) US ARMY TEST AND EVALUATION COMMAND
A FOURNIER

1 (PDF) MTRL SCIENCES DIV
LAWRENCE BERKELY NATL LAB
R RITCHIE

1 (PDF) SOUTHWEST RSRCH INST
C ANDERSON JR
S CHOCRON
D NICOLELLA
T HOLMQUIST
G JOHNSON

2 (PDF) NIST
A FORSTER
M VANLANDINGHAM

1 (PDF) INST FOR DEFNS ANLYS
Y MACHERET

3 (PDF) MRMC DOD BLAST INJURY RSRCH PROGRAM COOR OFC
R GUPTA
T PIEHLER
R SHOGE

2 (PDF) MRMC JTAPIC PRGM OFC
W LEI
J USCILOWICZ

1 (PDF) WIAMAN PMO
K LOFTIS

4 (PDF) US ARMY AEROMEDICAL RSRCH LAB
F BROZOSKI
V CHANCEY
B MCENTYRE
D WISE

1 (PDF) DEVCOM GROUND VEHICLE SYSTEMS CENTER
R SCHERER

1 (PDF) DEVCOM
AMSRD PE
D RUSIN

2 (PDF) DEVCOM CHEMICAL BIOLOGICAL CENTER
M HORSMON
N VINCELLI

1 (PDF) OSD DOT&E
J IVANCIK

5 (PDF) US NAVAL RESEARCH LABORATORY
A BAGCHI
A ILIOPOULOS
J MICHOPOULOS
K TEFERRA
X TAN

3 (PDF) DEVCOM DAC
FCDD DAS LBW
G DIETRICH
FCDD DAS LBE
J GURGANUS
S SNEAD

86 (PDF) DEVCOM ARL
FCDD RLW
S KARNA
J NEWILL
A RAWLETT
S SCHOENFELD
J ZABINSKI
FCDD RLW B
R BECKER
J CAMPBELL
P GILLICH
C HOPPEL
B SCHUSTER
A TONGE
L VARGAS-GONZALEZ
FCDD RLW L
A DAGRO
A EIDSMORE
C GOOD
T V SHEPPARD
T THOMAS
FCDD RLW LF
T G BROWN
FCDD RLW LH
T EHLERS
L MAGNESS
C MEYER
D SCHEFFLER
FCDD RLW M
E CHIN
FCDD RLW MA
T BOGETTI
T PLAISTED
J SANDS
E WETZEL
M YEAGER
C YEN
FCDD RLW MB
G GAZONAS
B LOVE
P MOY
D O'BRIEN
J SIETINS
J SUN
T WALTER
FCDD RLW MC
R JENSEN
FCDD RLW MD
A BUJANDA
B CHEESEMAN
K CHO
J LA SCALA
S WALSH
FCDD RLW ME
J LASALVIA
P PATEL
S SILTON
J SWAB
FCDD RLW MF
K DARLING
S GRENDAHL
H MURDOCH
FCDD RLW MG
J ANDZELM
J LENHART
R MROZEK
FCDD RLW P
R FRANCART
FCDD RLW PA
S BILYK
FCDD RLW PB
S ALEXANDER
T BAUMER
A BROWN
B FAGAN
A GOERTZ
A GUNNARSSON
C HAMPTON
M KLEINBERGER
E MATHEIS
J MCDONALD
P MCKEE
K RAFAELS
S SATAPATHY
M TEGTMEYER
T WEERASOORIYA
S WOZNIAK
T ZHANG
FCDD RLW PC
J CAZAMIAS
D CASEM
J CLAYTON
C MEREDITH
L SHANNAHAN
J LLOYD
FCDD RLW PD
R DONEY
K MASSER
C RANDOW
FCDD RLW PE
M LOVE
P SWOBODA
FCDD RLW PF
N GNIAZDOWSKI
R GUPTA
S KUKUCK
FCDD RLW S
A WEST

4 (PDF) WHITING SCHOOL OF ENG
JOHNS HOPKINS UNIV
KT RAMESH
T D NGUYEN
B NOTGHI
S BAILOOR

2 (PDF) COULTER DEPT OF BIOMED ENG
GEORGIA INST OF TECH
S MARGULIES
D MCDOWELL

1 (PDF) DEPT OF ENGRNG SCI AND MECHANICS
VIRGINIA POLYTECHNIC INST AND STATE UNIV
R BATRA

3 (PDF) MASSACHUSETTS INST OF TECHLGY
INST FOR SOLDIER NANOTECHNOLOGIES
R RADOVITZKY
S SOCRATE
M J BUEHLER

1 (PDF) DEPT OF MECHL AND NUCLEAR ENGRNG
THE PENNSYLVANIA STATE UNIV
R KRAFT

1 (PDF) INDIAN INST OF TECH
R BHARDWAJ

2 (PDF) CENTER FOR APPLIED BIOMECHANICS
UNIV OF VIRGINIA
R SALZAR
M B PANZER

1 (PDF) UCSD MAT SCI AND ENG
MARC MEYERS

1 (PDF) DUKE UNIV
BIOMED ENG
CR BASS

1 (PDF) UNIV OF CAPE TOWN
BLAST IMPACT & SURVIVABILITY UNIT
TJ CLOETE

1 (PDF) UNIV OF OXFORD
BLAST IMPACT & SURVIVABILITY UNIT
C SIVIOUR

1 (PDF) UNIV OF CAMBRIDGE
ENG DEPT
V DESHPANDE

2 (PDF) UNIV OF SOUTH CAROLINA
COL OF ENG
S RAJAN
M SUTTON
S SOCKALINGAM
F THOMAS

1 (PDF) IMPERIAL COL LONDON
DEPT OF PHYSICS
W PROUD

1 (PDF) DIV OF ENG AND APPL SCI
CALTECH
R RAVICHANDRAN

1 (PDF) DEPT OF AERO ENG AND ENG MECH
U TEXAS AUSTIN
K RAVI-CHANDAR

1 (PDF) AERO AND ASTRO ENG
PURDUE UNIV
W CHEN

1 (PDF) DEPT OF NEUROSURGERY
MED COL OF WISCONSIN
N YOGANANDAN

1 (PDF) SANDIA NATL LAB
B SANBORN